Controlling Exciton Polarization in Transition Metal Doped Indium Oxide Nanocrystals

by

Qinghao Shao

A thesis

presented to the University of Waterloo

in fulfillment of the

thesis requirement for the degree of

Master of Science

in

Chemistry

Waterloo, Ontario, Canada, 2024

Author's Declaration

I hereby declare that I am the sole author of this thesis. This is a true copy of the thesis, including any required final revisions, as accepted by my examiners.

I understand that my thesis may be made electronically available to the public.

Abstract

The simultaneous manipulation of electronic charge and spin in dilute magnetic semiconductors (DMSs) doped with transition metal ions has been long considered a holy grail for advancing spintronics and quantum information processing technologies. Although room temperature (RT) ferromagnetism has been attained in multiple DMSs including DMS oxides (DMSOs), these results have inconsistency in reproducibility. Moreover, RT ferromagnetism has also been observed in several metal oxides in the absence of any transition metal dopants. This phenomenon has been attributed to intrinsic defects in the host lattice, which creates confusion over the nature of exchange interactions that lead to RT ferromagnetism in DMSs. Here, using a carefully designed series of Co^{2+}-doped indium oxide (Co^{2+}:In_2O_3) nanocrystals (NCs) with different doping concentrations, and employing magnetic circular dichroism spectroscopy, we unravel the dominant mechanism governing spin polarization of charge carriers as a function of doping concentration, and establish the contributions of intrinsic defects and dopants to Zeeman splitting in Co^{2+}:In_2O_3 NCs. Furthermore, the exchange coupling between the excitonic states and Co^{2+} is strongly dependent on the NC volume for sizes approaching the quantum confinement regime, but largely independent on the radial position of the dopants for larger NCs due to spatially homogeneous wavefunction of the exciton. Our work provides a critical understanding on why DMSOs are so sensitive to the synthesis methodology and will aid in developing new DMSO NC systems whose magnetic properties can be consistently predicted and reproduced.

Acknowledgements

Firstly, I would like to express my heartfelt gratitude to my supervisor, Dr. Pavle Radovanovic, who not only provided me with the opportunity to embark on this research journey but also guided me with invaluable insights and unwavering support.

I would also like to thank my advisory committee members, Dr. Holger Kleinke and Dr. Vivek Maheshwari. Their guidance, constructive feedback, and expert advice have been instrumental in shaping and refining my research work. Their perspectives and suggestions have greatly improved my thesis writing.

Additionally, special thanks are given to all members of the Pavle's group for their support. The support and collaboration within the group have been a source of constant encouragement.

Last but certainly not least, my deepest gratitude is for my parents. Their unwavering understanding and support have been the bedrock of my journey. Their love and belief in me have been a constant source of strength and motivation, enabling me to pursue and achieve my goals.

Table of Contents

List of Figures

List of Tables

List of Abbreviations

ac	Acetate
acac	Acetylacetonate
bcc	Body-centered cubic
BMP	Bound magnetic polaron
CB	Conduction band
Co^{2+}:In_2O_3	Cobalt(II)-doped indium oxide
DMS	Diluted magnetic semiconductor
DMSO	Diluted magnetic semiconductor oxide
FCE	F-center exchange
FWHM	Full width at half maximum
GMR	Giant magnetoresistance
HR-TEM	High-resolution transmission electron microscopy
ICP-OES	Inductively coupled plasma-optical emission spectroscopy
LCP	Left circularly polarized
MCD	Magnetic circular dichroism
NC	Nanocrystal
Ni^{2+}:In_2O_3	Nickel(II)-doped indium oxide

RCP	Right circularly polarized
rh	Rhombohedral
RKKY	Ruderman-Kittel-Kasuya-Yosida
RT	Room temperature
T_C	Curie temperature
TCO	Transparent conducting oxide
TEM	Transmission electron microscopy
TOPO	Trioctylphosphine oxide
UV-Vis	Ultraviolet-visible
UV-Vis-NIR	Ultraviolet-visible-near infrared
VB	Valence band
XRD	X-ray diffraction

Chapter 1

Introduction Section

1.1 Multifunctional Material

Over the past few decades, the studies of multifunctional materials have attracted much interest in material science. Such materials could integrate various functional properties within a single system, including optical, magnetic, and electronic characteristics.[1] By investigating the combination and correlation among these relevant properties, researchers have the potential to manipulate and fine-tune them within the material framework.[2] Thus, starting with conventional materials, multifunctional materials are specifically developed to reduce of eliminate existing material limitations and broaden the scope of their applications.

1.1.1 Spintronics

Spintronic materials, a distinct category within multifunctional materials built upon the foundation of conventional semiconductors, are regarded as the next generation of advanced materials for electronic devices for information storage and processing.[3–5] As the traditional semiconductor-based electronics rely on the movement of electrons in the transistors, the physical limitations of transistors' size and packing are being approached. In contrast, the spintronics, or spin-electronics, focuses on devices that utilize electron spin manipulation in addition to charge, allowing for a much faster data processing speed, reduction in device size, and higher energy efficiency.

The spintronics studies focus on controlling and manipulating spin degree of freedom in solid-state systems, which can attain two distinct states, resulting in a significant difference in

electrical resistance. The giant magnetoresistance (GMR) effect was discovered by Albert Fert and Peter Grünberg in 1988.[6] According to the GMR theory, in a structure of a non-magnetic layer sandwiched between two ferromagnetic layers, the resistance differences correspond to the alignment of the magnetization in the ferromagnetic layers.[7] The magnetic moments are typically parallel or antiparallel, resulting in low and high electrical resistances, respectively. These two states can be represented as "on" and "off" in spintronic devices. Therefore, the ability to switch between these two states allows for faster data processing speed with lower energy consumption compared to conventional electronic devices.[3]

1.2 Semiconductor

Semiconductors are a specific kind of material exhibiting an electrical conductivity between conductors and insulators.[8] For different materials, electrical conductivities can be correlated with their band gap energies, using the band structure model. Figure 1.1 illustrates the band structures of different kinds of materials. The band gap refers to the energy gap located between the highest level of the valence band (VB), which is the occupied band state, and the lowest level of the conduction band (CB), where the electronic states are typically unoccupied. For an insulator, there is a large band gap (typically greater than 5 eV), which prevents electronic transition from VB to CB in the absence of high energy photons. In contrast, conductors exhibit overlap between VB and CB, allowing the electrons to move freely throughout the material. In semiconductor materials, the moderate band gap separates the CB and VB, restricting the free electron movement under normal conditions. But with appropriate external energy, the electrons can be excited across the band gap to higher energy levels.

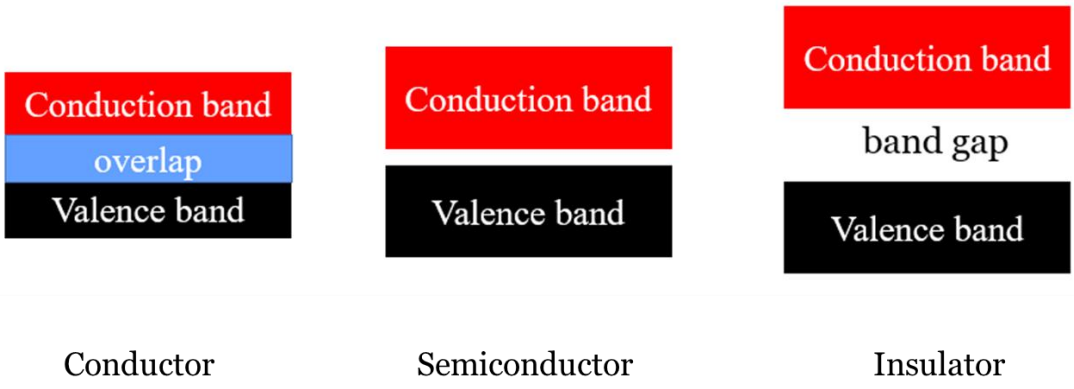

Figure 1.1 Schematic diagram of the electronic bands, including conduction band (CB) and valence band (VB), and their separation for a conductor, semiconductor, and insulator.

Semiconductor materials are broadly classified into two main categories: intrinsic and extrinsic semiconductors. Intrinsic semiconductors, such as Si and Ge, have a pure composition with no dopant impurities. However, due to the limited application of intrinsic semiconductors, the extrinsic semiconductors are obtained by introducing a small amount of impurities into the semiconductor host lattice. Based on the nature of the impurity dopants, the extrinsic semiconductor can be further divided into *n*-type and *p*-type. Figure 1.2 displays the band structures for both *n*- and *p*-type semiconductors. The *n*-type dopants can donate valence electrons to the CB and establish an electron donor level near the CB, while the *p*-type dopants can provide electron holes to accept the electrons from the VB, creating an electron acceptor level close to the VB. The charge carriers in the *n*-type and *p*-type semiconductors are the negative electrons and positive electron holes, respectively.

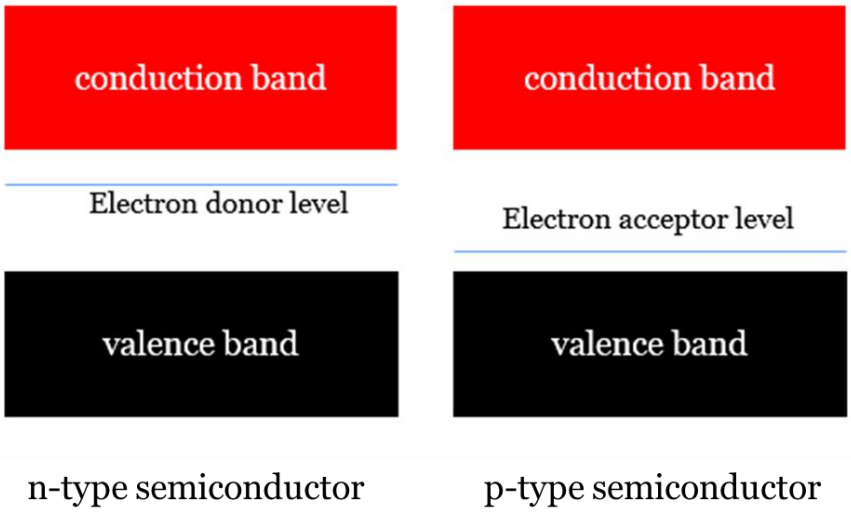

Figure 1.2 The schematic diagram of the band structure of *n*-type (left) and *p*-type (right) semiconductor.

1.2.1 Diluted Magnetic Semiconductor

Diluted magnetic semiconductors (DMSs) are a specific class of multifunctional materials, which combine both semiconducting and magnetic properties within one material system.[9] This combination makes the DMSs promising candidate materials for spintronic devices, due to the ability to simultaneously manipulate the electronic charge and spin properties in semiconductor materials.[10]

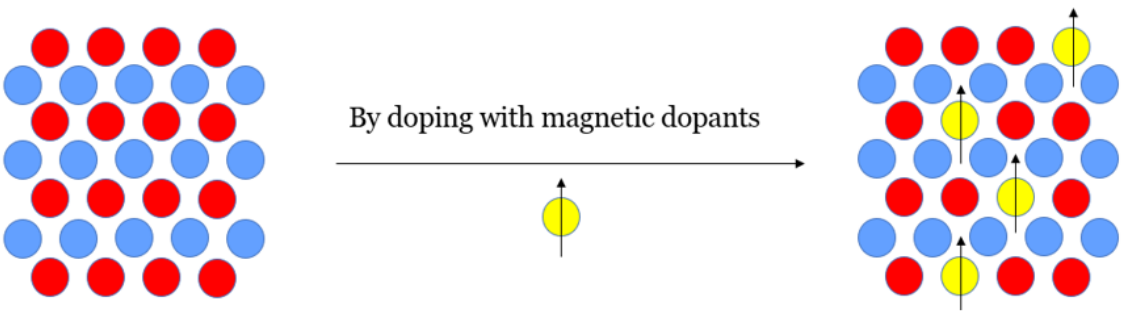

Figure 1.3 Schematic representation of a DMS material based on the non-magnetic semiconductor host lattice and magnetic dopants (usually transition metal ions with unpaired *d*

electrons).

To produce a DMS, a small amount of transition metal ions with a high magnetic moment are introduced into conventional non-magnetic semiconductor host lattice as impurity dopants. Generally, the doping percentage is limited to around 15% to avoid significant distortion of the host lattice structure and secondary phase formation.[9]

The magneto-optical and magneto-electrical properties of the host material can be induced by the exchange interactions between the unpaired *d* electrons of the transition metal dopants and *s* or *p* electrons of host lattice. [11] As a variety of studies of DMSs have been investigated based on the II-VI (e.g., CdSe) and III-V (e.g., GaAs) semiconductor systems,[12–16] the spin exchange interactions are referred to the *sp-d* exchange interactions, owing to the *s*-orbital nature of the conduction band and *p*-orbital nature of the valence band interacting with *d*-orbitals of the transition metal dopants.[17,18]

Through the substitution with magnetic ions, DMSs may also exhibit ferromagnetic properties below the Curie temperature (T_C), which is known as the ferromagnetic phase transition temperature.[19] Above the T_C, such DMSs undergo a phase transformation from ferromagnetic to paramagnetic. However, the T_C of most ferromagnetic DMSs is lower than room temperature, which dramatically limits their applications. Thus, one of the most significant challenges in this field is to develop high-T_C DMSs, which would be suitable for spintronic applications above room temperature.[20]

As illustrated in Figure 1.4, several models of DMS have been created to explain the magnetism in the context of its band structure.[21] The first possibility is donor doping, such as the Gd-doped

EuO, which places a carrier in the spin-polarized conduction band. The carriers are delocalized below T_C but form magnetic polarons above T_C. The other type of semiconductor is acceptor doping, as Mn substitutes into the GaAs lattice, where the Mn ion introduces occupied 3*d* states below the maximum of the As 4*p* valence band, and the ferromagnetism is mediated by 4*p* acceptor holes that are polarized by exchange with the $3d^5$ Mn^{2+} ion.

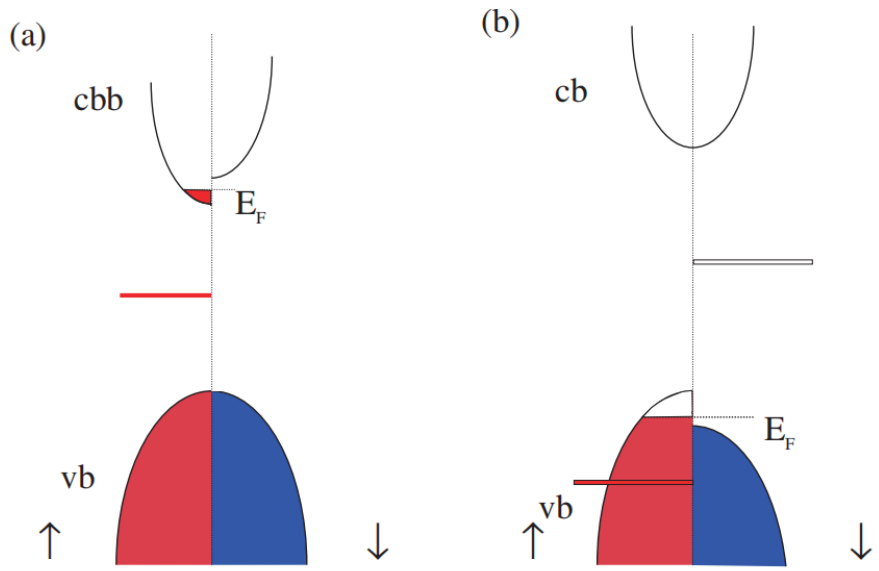

Figure 1.4 Two schematic models for band splitting in typical DMSs: spin-split conduction band (left), spin-split valence band (right).[21]

1.3 Transparent Conducting Oxide

Transparent conducting oxide (TCO) is one of the most attractive semiconductor materials characterized by a wide band gap (typically above 3.5 eV), which results in low absorption in the visible region. TCOs, such as ZnO, TiO_2, and In_2O_3, exhibit a remarkable combination of optical transparency (> 80%) to visible light and electrical conductivity ($\sim 10^3$ $\Omega^{-1}cm^{-1}$).[22,23] Besides, TCOs are more cost-effective and chemically stable compared to other semiconductors. Such an impressive combination of properties of TCOs has attracted extensive research interest

in the past decade with a wide range of applications, including solar cells, optoelectrical devices, and smart windows. By controlling the doping elements with their concentrations, the electrical and optical properties of TCOs can be easily tuned. Furthermore, recent studies have revealed that intrinsic structural defects, such as oxygen vacancies, can also be utilized to manipulate the optical, magnetic, and electrical properties in TCOs.[19,24]

1.3.1 Diluted Magnetic Semiconductor Oxide

In addition to the traditional II-VI and III-V semiconductors, TCOs have been regarded as one of the most promising host lattices for DMS materials. This is largely due to their advantageous combination of properties, including electrical conductivity and mobility, visible transparency, abundance, stability, and non-toxicity.[25–30] As they are based on wide band gap semiconductor oxides, this specific type of DMS material is known as diluted magnetic semiconductor oxides (DMSOs).

Since the first observation of room-temperature ferromagnetism in Co-doped TiO_2,[20] the interest in developing DMSO materials with high T_C has dramatically increased, as it can eliminate the limitations in high-temperature spintronics applications. Unfortunately, it has proven challenging to consistently reproduce magnetic properties of DMSO materials, where the samples having the same composition but prepared by different synthetic techniques or different research groups have shown drastically different magnetic behavior.[18,31–33] Recent studies indicated that intrinsic structural defects such as oxygen vacancies can play an important role in manipulating the magnetic behavior of the DMSOs.[19,34] It has been shown that unpaired electrons localized on oxygen vacancies may also undergo spin exchange interactions with

conduction band states in metal oxide NCs, acting as a source of carrier polarization in analogy to transition metal dopants in DMSOs.[24] This result shines a new light on the possible origin of "d^0" ferromagnetism at room temperature observed in a number of non-magnetic transparent conducting oxides including HfO_2,[35] CeO_2,[36] In_2O_3,[37,38] ZnO,[34,39,40] and TiO_2[31,41] in the absence of any transition metal dopants. Therefore, the correlation between band splitting induced by the native oxygen vacancies and transition metal dopants becomes an interesting research aspect for deep understanding of magnetic behavior within DMSO materials.

Several assumptions such as bound magnetic polaron (BMP) theory,[42,43] Ruderman-Kittel-Kasuya-Yosida (RKKY) exchange interaction models,[44,45] and F-center exchange (FCE) model,[46] have been proposed to explain the origin of ferromagnetism in these materials. Among all the mechanisms, one of the most acceptable models is BMP model, which describes well the magnetic behavior in defective materials.[42] As indicated in the Figure 1.5, in the BMP model, the 3*d* transition metal ions randomly substituted for semiconductor cation sites and the inherent oxygen vacancies which act both as electron donors and as electron traps, can interact. The unpaired electrons on dopant centers can then align, leading to a bound polaron with a large magnetic moment.[43] The bound magnetic polarons can mediate the magnetic order within the DMSO material. The exchange interaction between bound polarons dramatically decreases with the increase in distance. As the bound magnetic polarons are randomly separated, the strength of interaction will be mainly determined on the concentration of magnetic polarons, which correspond to the concentration of magnetic dopants and the oxygen vacancies. The low donor concentration and weak exchange interaction will lead to the localized isolated polarons displaying paramagnetic behavior, while the strong exchange interaction will lead to overlapped

polarons and ferromagnetic behavior.

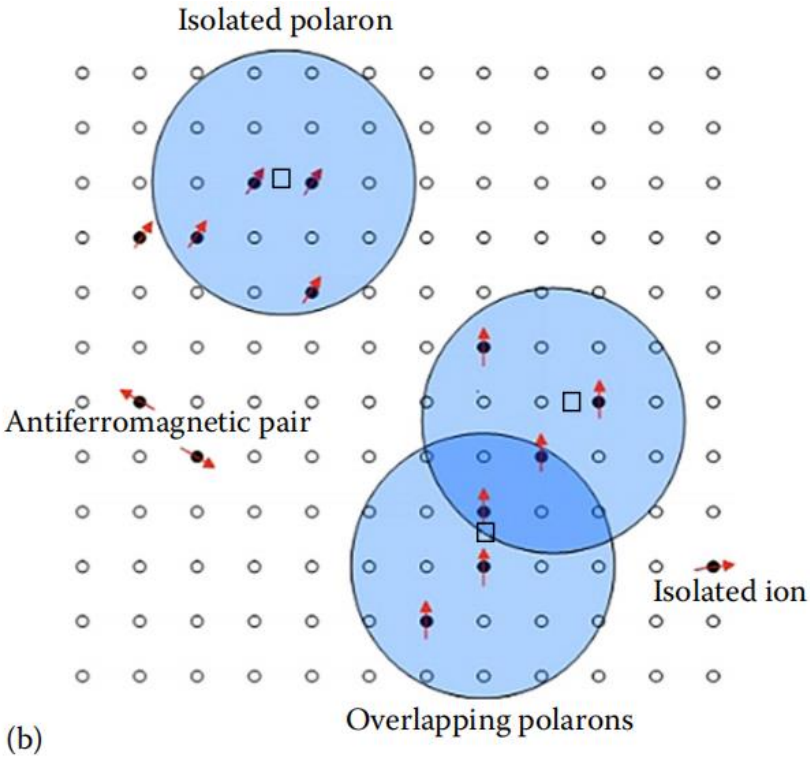

Figure 1.5 Schematic representation of random distribution of dopant ions and oxygen vacancies that generate bound magnetic polarons, and the exchange interaction between polarons.[42]

1.3.2 Indium Oxide

Indium oxide (In_2O_3) is a typical *n*-type intrinsic semiconductor with a wide band gap of around 3.75 eV.[19] As one of the most interesting TCO systems, In_2O_3 has been widely investigated as an optoelectronic and DMSO host-lattice material.[47] The indium oxide adopts two main structures: the stable phase of body-centered cubic (bcc) bixbyite-type structure with the space group $Ia\bar{3}$ (No. 206) and the metastable phase of rhombohedral (rh) corundum-type structure with the space group $R\bar{3}c$ (No. 167).[47] During the synthesis, the metastable rh structure is the intermediate phase, and the phase transformation can be achieved through

applying higher temperature which eventually turns into it the stable cubic-phase In_2O_3.[48,49] Based on previous research, most researchers focused on the bcc structure to make the In_2O_3 NCs more stable and phase-pure.[19,47,50–52]

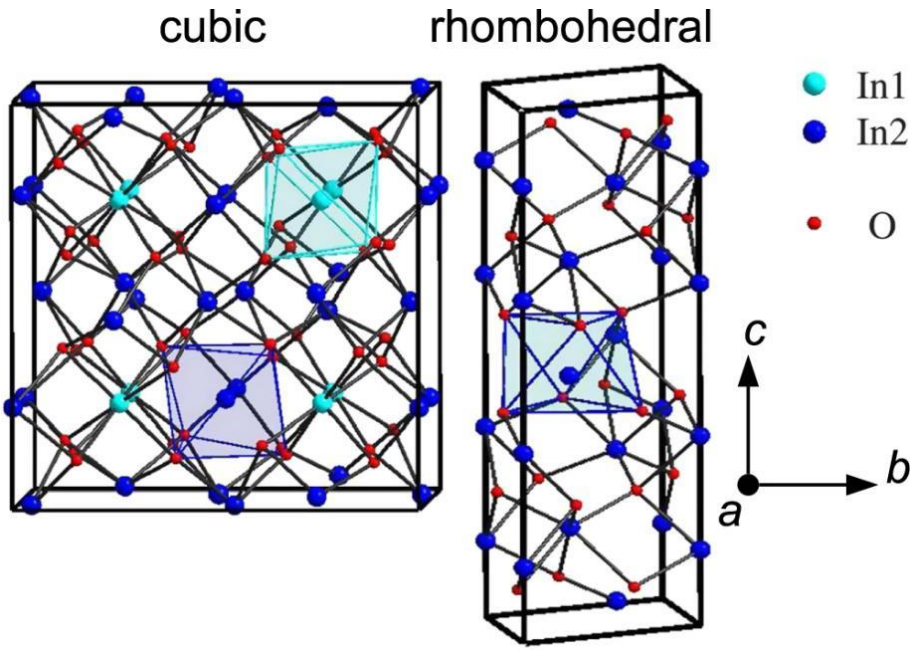

Figure 1.6 The cubic structure (left) and rhombohedral structure (right) of indium oxide crystal lattice.[51]

As illustrated in Figure 1.6, the cubic cell contains 80 atoms, 48 oxygen atoms and 32 indium atoms, occupied in the anion and cation sites, respectively.[53] Among all cation sites, it a quarter (8) are *b* sites and three-quarters (24) are *d* sites. The *b* site has a slightly trigonally compressed octahedral coordination with six identical bond lengths and S_6 site symmetry, while the *d* site is a highly distorted octahedral site with three sets of bond lengths and C_2 site symmetry.[52,54,55] In In_2O_3, the intrinsic defect, especially oxygen vacancy, is the major donor and creates a donor state producing free electrons in the conduction band, which makes the undoped Indium oxide perform high *n*-type semiconductor. The high electron mobility, carrier

density, and wide bandgap make In_2O_3 superior to the other TCOs as the host lattice for DMSOs.[29]

1.4 Magnetic Circular Dichroism Spectroscopy

Magnetic Circular Dichroism (MCD) spectroscopy is a specific technique used for investigating the magneto-optical properties of various NC samples. The MCD signal intensity can be determined based on the difference in the absorption between left circularly polarized (LCP) light and right circularly polarized (RCP) light in a sample induced by a strong magnetic field parallel to the direction of light propagation. [56] This absorption disparity can be described by the convention as

$$\Delta A = A_- - A_+ \qquad \textbf{(Equation 1.1)}$$

where A_- and A_+ represent the absorptions by LCP and RCP, respectively.[57] The ΔA in MCD originates from the Zeeman splitting of the ground and excited states. The MCD intensity of for a transition from the ground state $|A\rangle$ to an excited state $|J\rangle$ is described in the following equation [56]:

$$\frac{\Delta A}{E} = \left(\frac{2N_0\pi^3\alpha^3 Cl\log(e)}{250hcn}\right)\mu_B B\left[A_1\left(-\frac{\partial f(E)}{\partial E}\right) + \left(B_0 + \frac{C_0}{kT}\right)\right] f(E) \qquad \textbf{(Equation 1.2)}$$

where ΔA is from the differential absorption calculated through the Equation 1.1, $E = \hbar v$, α is the electric permeability, C is the concentration, l is the path length, n is the index of refraction, μ_B is the Bohr magneton, B is the external applied magnetic field. The A_1, B_0, and C_0 represent the MCD *A*-, *B*-, and *C*-term, respectively. $f(E)$ is the absorption spectrum band shape, and $\frac{\partial f(E)}{\partial E}$ is its first derivative. Under external magnetic field along the light propagation direction, the ground state and/or the excited states are split due to Zeeman

perturbation with a magnitude of

$$-\mu_z B = \mu_B\left(g_L \hat{L}_z + g_S \hat{s}_z\right)B \qquad \textbf{(Equation 1.3)}$$

where $\hat{L}_z$ and $\hat{s}_z$ are the orbital and spin angular momentum operators, respectively, and g_L = 1 and g_S = 2.002 are the corresponding gyromagnetic ratios. The overall electron angular momentum responsible for the electron polarization is $J = L + S$, with the MCD selection rule $\Delta M = \pm 1$ (+/-1 represent the left/right circular polarized light, respectively).[56]

In MCD, the *A*-term occurs in the system which has degenerate excited states. Under magnetic field, the excited states are split due to the Zeeman effect. This splitting, typically only a few wavenumbers, leads to the formation of two oppositely signed absorption bands that combine to produce a derivative shape MCD signal, as illustrated in Figure 1.7.

Conversely, *C*-term MCD is observed in systems with degenerate ground states, which also undergo Zeeman splitting in the presence of an external magnetic field. At low temperatures, kT is comparable to or less than the Zeeman splitting magnitude with applied external magnetic field, leading to the Boltzmann population of the lower ground state sublevel being larger than that of the higher-energy sublevel. This imbalance in population results in two oppositely signed absorption bands of different intensities, creating a predominantly absorption band-shaped signal displayed in Figure 1.7. *C*-term intensity is generally observed for MCD spectra of DMSO material.[58]

For the last *B*-term MCD, it is caused by the field-induced mixing of states. As described in Figure 1.7, this occurs when a third state, denoted as |K⟩, is energetically close to either the excited state |J⟩ or the ground state |A⟩, leading to significant Zeeman coupling. With the

increase in the intensity of the magnetic field, the degree of state mixing enhances, which then manifests as an absorption band-shaped signal in the MCD spectrum. Similar to the *A*-term, the *B*-term is typically temperature independent. However, temperature-dependent intensity of *B*-term signals may sometimes be observed, particularly when the state |K⟩ is relatively low-lying in energy.

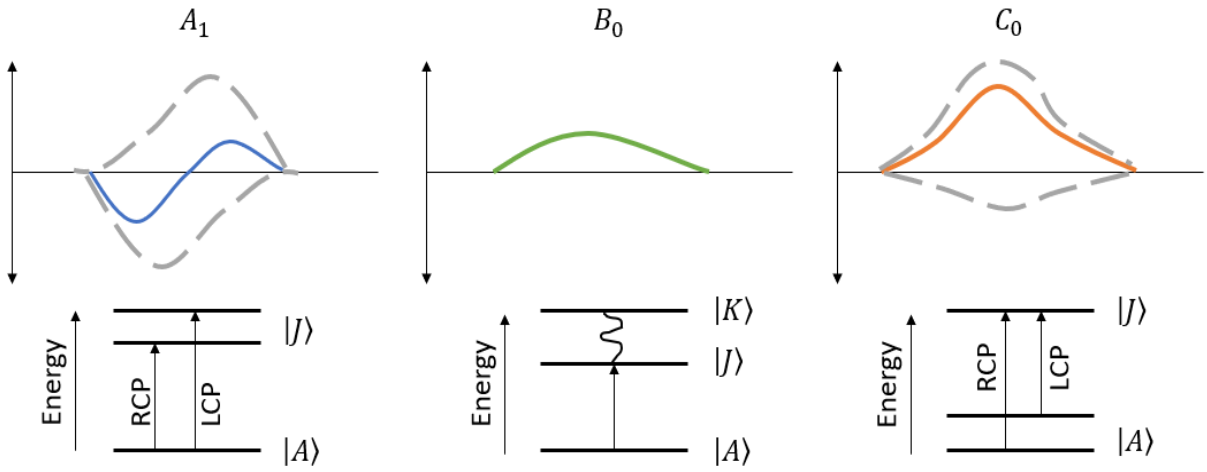

Figure 1.7 Schematic diagram of MCD terms with MCD signal (top) and Zeeman splitting (bottom) for *A*-term, *B*-term, and *C*-term MCD.[59]

1.5 Motivations and Scope of the Thesis

In addition to II-VI and III-V semiconductors, the wide band gap metal oxide semiconductors are also regarded as promising host lattices for commercial DMSs due to their favorable combination of electrical conductivity and mobility, transparency, abundance, stability, and non-toxicity. One of the likely reasons for the discrepancies of the reported magnetic properties of DMSOs is the presence of native defects which are sensitive to sample preparation and processing conditions. Notably, oxygen vacancies that have been proposed to play an important role in several proposed mechanisms of ferromagnetic ordering. Recent

results have shown that unpaired electrons localized on oxygen vacancies may also undergo spin exchange interactions with conduction band states in metal oxide NCs, acting as source of carrier polarization in analogy to transition metal dopants in DMSOs. Therefore, this thesis aims to delve into the intricate correlation between band splitting induced by native defects and transition metal dopants in this class of materials. By examining the related magneto-optical properties, the research seeks to contribute to the understanding of DMSOs, paving the way for their effective implementation in future spintronic applications.

To be more specific, in this thesis work, I proposed a modified synthesis method for preparing colloidal transition metal (cobalt) doped In_2O_3 NCs, which is a typical DMSO material, and explored magnetic exchange interactions in Co^{2+}-doped In_2O_3 (Co^{2+}:In_2O_3) NCs with varying Co^{2+} doping concentrations using MCD spectroscopy. Then I compared the MCD spectra of pure In_2O_3 and Co^{2+}:In_2O_3 NCs and investigated the evolution of exciton polarization for increasing Co^{2+} doping concentration. The spectroscopic results reveal that band splitting in low-doped NCs is dominated by exchange interactions involving singly-charged oxygen vacancies in the presence of an applied magnetic field. With increasing Co^{2+} doping level, the dopant-induced exchange interactions take over as the dominant mechanism governing the anomalous Zeeman splitting of the NC band states. Surprisingly, the two types of exchange interactions are found to be comparable in magnitude but result in the opposite splitting pattern of the band states, leading to cancelation of the MCD signal for Co^{2+} doping concentration between ca. 0.3 and 0.5%. The results of this work suggest that exchange interactions in DMSOs are more complex than typically modelled, and that localized intrinsic defects play a key role in the observed magneto-optical and magnetic properties. The interplay between exchange

interactions elucidated in this work may help explain some inconsistent results reported in the literature, and allows for the design of DMSO NCs with optimal magneto-optical properties.

Additionally, to further investigate the effects of Co^{2+} dopant locations on the excitonic Zeeman splitting in Co^{2+}:In_2O_3 NCs, I prepared two specific types of core/shell NCs with Co^{2+} dopants either in the core or on the shell through a modified slow-injection method. Furthermore, compared to uniformly-doped Co^{2+}:In_2O_3 NCs at similar doping concentrations, the core/shell-structured samples exhibit significantly larger NC sizes. This size difference provides the opportunity to explore the impact of NC sizes on the magneto-optical properties of Co^{2+}:In_2O_3 NCs. Through the synthetic control of the NC size and dopant locale, we have presented evidence that the excitonic Zeeman splitting in In_2O_3 NCs is highly sensitive to the NC volume, showing an order of magnitude higher MCD signal in uniformly-doped colloidal NCs up to ca. 5 nm in size, and negligible dependence of MCD signal on the radial location of the dopants for larger NCs.

Based on the research in this thesis, future research will focus on further investigation of the magneto-optical properties and excitonic polarization by replacing the cobalt ion with other transition metal ions to obtain a general understanding of the interplay of exciton polarization between intrinsic and extrinsic defects.

Chapter 2

Experimental Section

2.1 Materials

All chemicals were used as received from suppliers without any further purification. Indium(III) acetylacetonate ($In(acac)_3$, 98%), Indium(III) acetate ($In(ac)_3$, 99.99+%), Cobalt(II) acetylacetonate hydrate ($Co(acac)_2 \cdot xH_2O$, 98+%), and Cobalt(II) acetate tetrahydrate ($Co(ac)_2 \cdot 4H_2O$, 98+%) were purchased from Strem Chemicals. Oleylamine (70%) was obtained from Sigma-Aldrich, while oleic acid (90%), oleyl alcohol (85%) were supplied by Thermo-Fisher Scientific. Hexane (>99.9%), ethanol (90%) served as solvents for washing the NCs and preparing colloidal dispersions acquired from Fischer Chemical.

2.2 Synthesis and Samples Preparation

2.2.1 Synthesis of Colloidal In_2O_3 NCs

Colloidal In_2O_3 NCs were synthesized by modifying a previously published procedure for cubic-phase In_2O_3 NCs[50,51,60]. Using a standard Schlenk line apparatus, 1 mmol of $In(acac)_3$ and 10 mL of oleylamine were mixed in a 100 mL round bottom flask and purged with N_2 atmosphere for 5 minutes at room temperature. Subsequently, under vacuum conditions, the temperature was raised to 100 °C, and the system was degassed for 30 minutes. The reaction mixture was then gradually heated to 220 °C and kept undisturbed for 3 hours with continuous stirring under N_2 atmosphere.

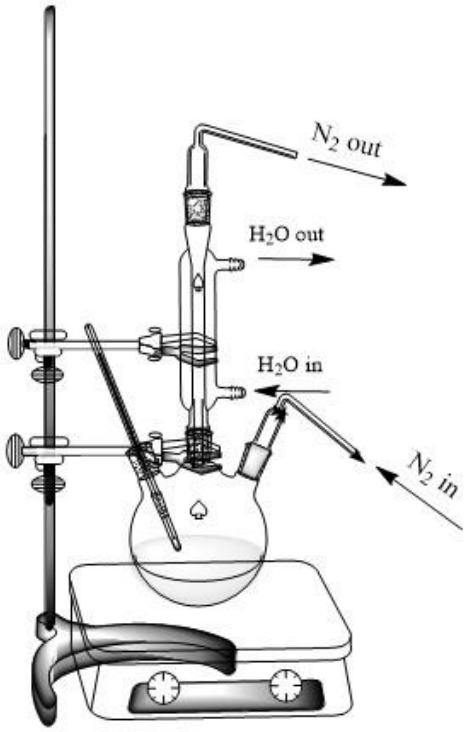

Figure 2.1 The reaction apparatus for colloidal synthesis of In_2O_3 NCs, including round bottom flask, condenser, thermometer, heating mantle and stirring plate.

The reaction mixture was allowed to air cool to room temperature upon completion. The resulting NCs were precipitated by adding an excess amount of ethanol, followed by centrifugation at 7,500 rpm for 5 minutes. The obtained precipitates were redispersed in hexane and washed with ethanol three times to remove all unreacted precursors and intermediates before finally dispersing them in a non-polar solvent, such as hexane, for various characterization techniques.

2.2.2 Synthesis of Uniformly-Doped Co^{2+}:In_2O_3 NCs

For the synthesis of Co^{2+}:In_2O_3 NCs, the procedure was modified to introduce cobalt dopants into the host lattice. Along with $In(acac)_3$ as the Indium precursor, a stoichiometric amount of cobalt precursor, $(Co(acac)_2 \cdot xH_2O)$, was added to the reaction mixture. The reaction

conditions during the synthesis step and subsequent precipitation and purification procedure were identical to the undoped synthesis. The final NC products were redispersed in hexane and other nonpolar solvents for further analysis.

For the additional surface treatment, the washed Co^{2+}:In_2O_3 NCs were treated with trioctylphosphine oxide (TOPO) at 90 ℃ for 1 h and precipitated with ethanol. Then the surface treatment was repeated twice to remove all surface bound cobalt ion.

2.2.3 Synthesis of Shell-Doped Co^{2+}:In_2O_3 NCs

The core-shell structure of Co^{2+}:In_2O_3 NCs, featuring either a doped core with an undoped shell or vice versa, was achieved through a modified slow-injection method originally developed by the Hutchinson group.[58,61] To start with the preparation of undoped core, a precursor solution was prepared by mixing stoichiometric amounts of indium acetate (III) and cobalt (II) acetate with oleic acid in a round-bottom flask to form a 0.5 M solution. The reaction mixture was initially degassed at ambient temperature for 10 minutes under vacuum and then heated to 100 °C for 30 minutes to form a metal-oleate complex. After switching to the N_2 atmosphere, the temperature was increased to 150 °C and maintained for another 2 hours with continuous stirring. Meanwhile, in a separate round-bottom flask, 13 mL of oleyl alcohol was heated to 290 °C under nitrogen. Hereafter, 2 mL of the prepared metal oleate solution was slowly injected into the heated oley alcohol using a syringe pump at a rate of 0.2 mL/min. Upon completion of the slow injection, the reaction mixture was cooled down to room temperature under ambient conditions, and NCs were precipitated by adding an excess amount of ethanol (~30 mL) and centrifugating at 7800 rpm for 5 mins. Thereafter, the obtained core NCs were

then redispersed in 7.5 mL of hexane and reprecipitated using 3 mL of ethanol, followed by centrifugation at 7500 rpm for 5 minutes. This washing process was repeated thrice to purify the NCs, with a small amount of oleic acid and oleylamine (~1% of NC weight) added during each step to enhance the colloidal stability of the NC dispersion. The washed NCs cores were eventually redispersed in nonpolar solvent such as hexane for further characterization.

For shell growth on the NC cores, the cores (either doped or undoped) were mixed into 13 mL of oleyl alcohol in a round-bottom flask. Hexane was then evaporated from this solution via a two-step degassing process: first at 40 °C and then at 100 °C for 30 minutes, respectively. Thereafter, 2 mL of metal-oleate solution was injected to the oleyl alcohol at 290 °C under the same slow-injection method at 0.2 mL/min. The resulting core-shell NCs were isolated and purified with the same precipitation and washing procedure motioned above as applied for the core NCs. Finally, these recovered NCs were redispersed in hexane and other nonpolar solvents for further characterization.

2.3 Measurements and Data Analysis

2.3.1 Powder X-ray Diffraction

Powder X-ray diffraction (XRD) is a widely used characterization technique that can be used to identify the crystal structures and purity of unknown samples. XRD patterns of powder from different NC samples placed on a shallow aluminum sample holder were conducted using an INEL XRG 3000 diffractometer equipped with a position-sensitive detector and a Cu $K\alpha_1$ radiation source (λ = 1.5418 Å) in Dr. Holger Kleinke's group in the Department of Chemistry at the University of Waterloo.

Additionally, except for determining the unit cell parameters, the size of crystals can be estimated through the Debye-Scherrer equation, which is

$$\tau = \frac{K\lambda}{B\cos\theta} \quad \textbf{(Equation 2.1)}$$

Where τ is the average size of the determined crystal, K is a dimensionless shape factor with a value close to 0.9, λ is the wavelength of the Cu $K\alpha_1$ radiation source (1.5418 Å), θ is the Bragg angle in radians calculated from 2θ value at the peak position, B is the line width at the halfway of the maximum intensity (FWHM).

2.3.2 Transmission Electron Microscopy

Transmission electron microscopy (TEM), a critical tool for morphological analysis, facilitates a detailed determination of the morphology and polydispersity of different NCs. For specimen preparation, 20 μL of a dilute colloidal NC dispersion in hexane was deposited onto 300 mesh copper grids with lacey Formvar/carbon support films and dried in vacuum overnight. The TEM images were captured on a JEOL-2010F microscope operating at 200 kV for undoped In_2O_3 and uniformly doped Co^{2+}:In_2O_3 NCs, and core-shell Co^{2+}:In_2O_3 NCs images were collected by using a Zeiss Libra 200 MC microscope operating at 200 kV. TEM images for different NCs were later processed through ImageJ software and average NC diameter was obtained by fitting the size distribution of 100-200 NCs through a Gaussian fit function. The *d*-spacing measurement was carried out on the high-resolution TEM (HR-TEM) images.

2.3.3 Inductively Coupled Plasma-Optical Emission Spectroscopy

Inductively Coupled Plasma-Optical Emission Spectroscopy (ICP-OES) is a powerful analytical instrument used to determine the elemental composition of Co^{2+}:In_2O_3 samples on a

Teledyne Leeman Labs instrument. For the sample preparation, the NC samples were first digested in a freshly prepared Aqua-regia solution (3:1 HCl: HNO_3), and then diluted with milli-Q water to a final acid concentration of under 2% (v/v). Element quantification was achieved by comparing emission intensities against standard series prepared by diluting 1000 ppm commercial solutions to various concentrations, thus establishing the elemental percentage of the NCs.

2.3.4 Ultraviolet-Visible Absorption Spectroscopy

The ultraviolet-visible (UV-Vis) spectroscopy is a commonly used technique to analyze the material absorption in the UV-Vis region. The optical absorption spectra of different NCs dispersed in their hexane solution were collected on a Varian Cary 5000 UV-Vis-NIR spectrophotometer with a 1 cm pathlength Quartz cuvette. Meanwhile, the solid-state absorption spectra were carried out on NCs' thin films prepared by spin-coating the colloidal suspensions onto quartz substrates.

2.3.5 Magnetic Circular Dichroism Spectroscopy

MCD spectroscopy is a common method used to study the magneto-optical characteristics of NC materials. In this study, the MCD substrates were prepared by spin-coating dilute hexane dispersion of NCs onto strain-free quartz substrates. As shown in Figure 2.2, the MCD spectra were recorded using a Jasco J-815 spectropolarimeter in a Faraday configuration. When conducting the MCD measurement, the sample substrates were placed in an Oxford SM4000-8 superconducting magneto-optical cryostat, capable of varying temperature (1.5-300 K) and magnetic field strength (0-8 T). Upon passing through the samples, the combined elliptically

polarized beams were collected by the detector.

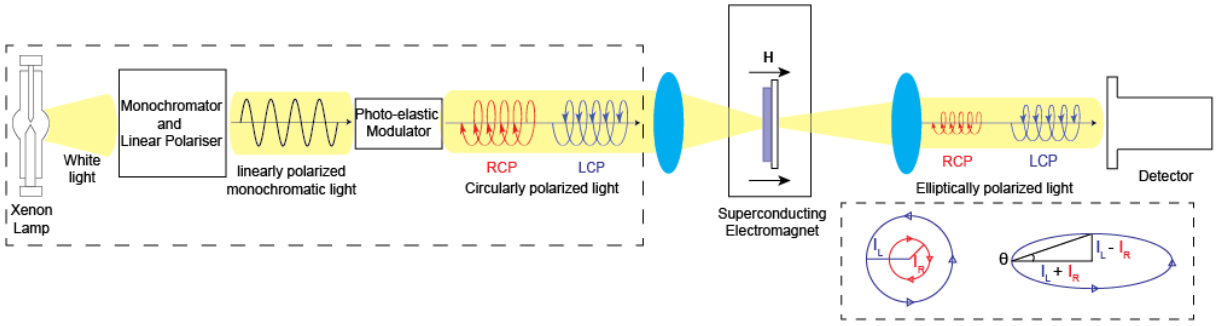

Figure 2.2 The schematic diagram of the experimental setup of MCD spectroscopy.[62]

The MCD spectroscopy's setup consists of three major parts, including the circularly polarized light generation part, the external magnetic field generation part, and the signal detector part. A light from Xenon lamp is passed through a monochromator and linear polarizer to generate a linearly polarized monochromatic light, and then it is passed through a photo-elastic modulator to create LCP and RCP beams. The lights passed through the sample substrates placed in the superconducting electromagnet to create an external magnetic field parallel to the light propagation direction. The differences of LCP and RCP lights are combined to form an elliptically polarized beam and collected by the detector with the degree of ellipticity, θ.

For the magnetic field dependence analysis, the MCD spectra were obtained at 5 K with field ranging from 0 T to 7 T at 1 T intervals. Then the original data was baselined by subtracting the 0 T signal. The integrated intensity of the MCD bands was calculated by determining the combined area under the positive and negative bands. These magnetic field dependence values were then fitted with a spin-only Brillouin function:

$$M_s = \frac{1}{2} N g_s \mu_B \left[(2S+1) \coth\left((2S+1) \frac{g_s \mu_B B}{2k_B T} \right) - \coth\left(\frac{g_s \mu_B B}{2k_B T} \right) \right] \quad \textbf{(Equation 2.2)}$$

In this equation, M_s stands for the sample's saturation magnetization, *N* for the carrier concentration as a fitting parameter, *S* for the spin quantum number, g_s for the Landé g-factor, *B* for the external magnetic field strength, k_B for the Boltzmann constant, μ_B for the Bohr magneton, and T for the temperature.

To compare the MCD intensities across different samples, the MCD spectra were normalized by converting the degree of ellipticity $\boldsymbol{\theta}$ to $\frac{\Delta \boldsymbol{A}}{\boldsymbol{A}}$ utilizing this following relationship[56]:

$$\frac{\Delta A}{A} = \frac{\theta}{32982 \times A} \quad \textbf{(Equation 2.3)}$$

Here θ is the MCD intensity obtained at 5 K under 7 T in millidegree, and A represents the corresponding absorbance of the NCs in the same range of MCD spectrum, as acquired by UV-Vis spectroscopy collected on Cary 5000 UV-Vis-NIR spectrophotometer.

The Zeeman Splitting energy for each sample can be estimated through the following equation 2.4 from the absorption and MCD spectra.[63,64]

$$\Delta E_z = \frac{\sqrt{2e}}{2} \sigma \frac{\Delta A'}{A_0} \quad \textbf{(Equation 2.4)}$$

Where $\Delta A'$ ($-\Delta A'$) represents the maximum amplitude at the positive (negative) peak of MCD feature, and A_0 corresponds to the maximum value of the related absorption peak and 2σ is the full Gaussian width of the absorption band at 1/e of the maximum absorbance (A_0).

Chapter 3

Study of Exciton Polarization in Cobalt-doped Indium Oxide Nanocrystals

In this chapter, I presented a modified synthesis method for colloidal Co^{2+}:In_2O_3 NCs and further explored the magnetic exchange interactions in these NCs with varying concentrations of Co^{2+} dopants through MCD spectroscopy. With the combination of structural and spectroscopic analyses, which includes XRD, TEM, ICP-AES, and UV-Vis absorption spectroscopy, I confirmed the successful incorporation of Co into In_2O_3 lattice without significant structural alterations. Furthermore, by comparing MCD spectra across different doping concentrations, I established the mechanism governing the spin-splitting of charge carriers with the contribution of intrinsic defects and extrinsic dopant impurities in Co^{2+}:In_2O_3 NCs.

3.1 Structural Characterization of In_2O_3 and Co^{2+}:In_2O_3 NCs

3.1.1 Elemental Analysis of Co^{2+}:In_2O_3 NCs

The synthesis of a series of colloidal Co-doped In_2O_3 NCs with varying starting dopant concentrations was prepared by a one-pot synthesis method at 220 °C using standard Schlenk line techniques as described above (check Experimental Sections 2.2.1 and 2.2.2 for more details)[50,51,60].

The actual Co doping concentrations for all samples were determined through ICP-OES measurements and were found to be in good agreement with the starting precursor concentrations. The agreement of the measured Co concentrations suggests that Co^{2+} ions are

readily incorporated into In_2O_3 NCs during the synthesis. The results of actual concentration of Co dopant in Co^{2+}:In_2O_3 NCs are summarized in Table 3.1 below.

Starting Precursor Ratio [Co]/[In] (%)	Actual Co Concentration [Co]/[In] (%)
0	0
0.5	0.32
2.5	1.97
5	3.73

Table 3.1 Summary of actual Co doping concentration in Co^{2+}:In_2O_3 NCs determined by ICP-OES measurement.

Furthermore, very similar doping concentrations were measured for Co^{2+}:In_2O_3 NCs, as synthesized, and upon their surface treatment with TOPO, which has been found to effectively remove transition metal dopants bound to the surfaces of metal oxide NCs.[25,30,65,66]

For accuracy and consistency, I will report all Co doping concentrations based on the values calculated by ICP-OES throughout this chapter.

3.1.2 Crystal Structure of In_2O_3 and Co^{2+}:In_2O_3 NCs

The powder XRD patterns were collected to characterize as-synthesized Co^{2+}:In_2O_3 samples by drop-casting the colloidal suspension of NCs onto the aluminum substrate. As illustrated in Figure 3.1, all NCs, across a range of doping concentrations, consistently exhibit a cubic bixbyite structure, as evidenced by matching to the XRD pattern for bulk bcc-In_2O_3 (JCPDS No.88-2160). This observation suggests that all Co^{2+}:In_2O_3 samples possess a high degree of phase purity without the formation of any observable secondary phase.

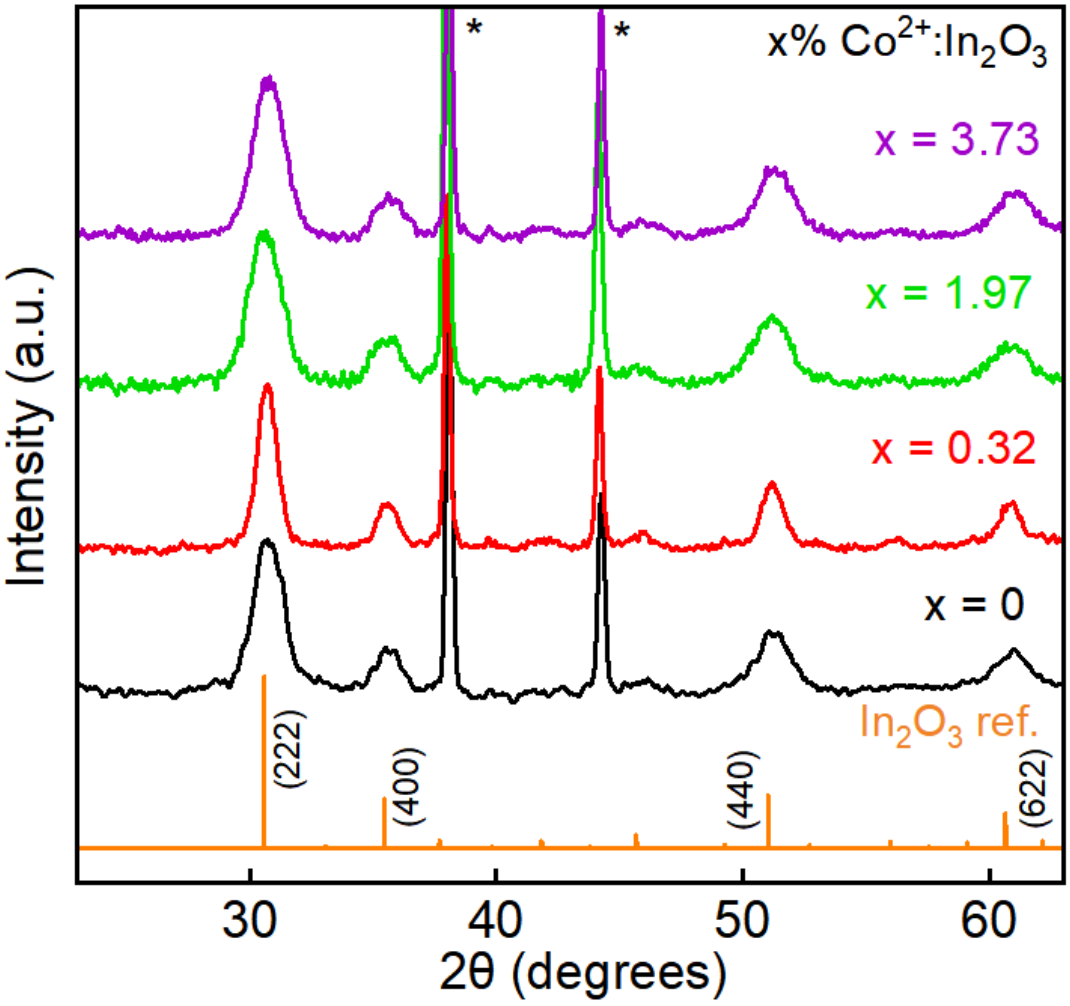

Figure 3.1 XRD patterns of Co^{2+}:In_2O_3 NCs with different Co doping percentages. Peaks marked with * represent the Al substrate. The vertical orange lines represent the XRD pattern for bulk cubic bixbyite phase In_2O_3 (JCPDS No.88-2160), with reflections from (222), (400), (440), and (622) planes indicated.

Additionally, as shown in Figure 3.1, the characteristic peaks corresponding to In_2O_3 lattice planes exhibited a trend of broadening with an increase in Co doping percentage. According to the Scherrer equation, the average particle sizes for all samples were estimated to be in the range of 6 to 10 nm, with a size decrease at high dopant concentrations. Such peak broadening and size reduction indicate the inhibition of NC growth during synthesis, likely due

to the presence of transitional metal impurities. [29,51,61,67,68]

3.1.3 Morphology Study of In_2O_3 and Co^{2+}:In_2O_3 NCs

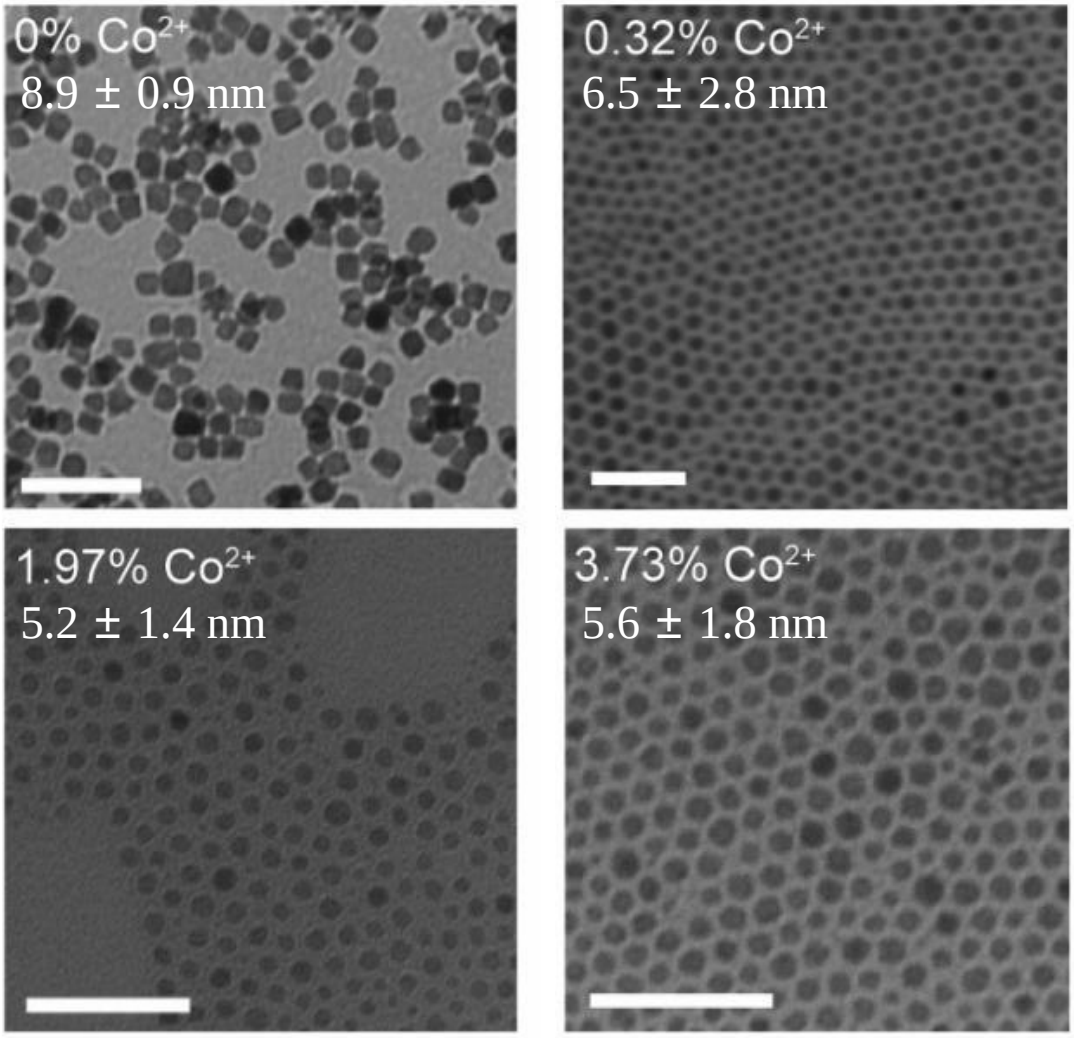

Figure 3.2 TEM images of Co^{2+}:In_2O_3 NCs with varying Co doping concentrations indicated in the figure. The average NC sizes are also shown as insets. All scale bars are 50 nm.

To confirm that Co substitution reduces the average NC diameter, the TEM measurements were obtained for as-synthesized Co^{2+}:In_2O_3 samples with varying doping percentages, as shown in Figure 3.2. It can be observed that all the NCs display square or quasi-spherical morphology with a relatively low polydispersity.

As the concentration of Co increases, there is a noticeable decrease in the average diameter of the NCs, from approximately 8.9 nm to 5.6 nm. This size reduction shows a good agreement with the estimated value obtained from the XRD pattern using the Scherrer equation, thus confirming the influence of Co^{2+} impurity on inhibiting the growth of In_2O_3 NCs. Taken together, TEM and XRD confirm that Co is substitutionally doped in the In_2O_3 lattice and does not participate in surface doping or segregation into secondary phases.

3.2 Optical Properties of In_2O_3 and Co^{2+}:In_2O_3 NCs

3.2.1 Optical Properties of the Band Gap in Co^{2+}:In_2O_3 NCs

To investigate the electronic structure of Co^{2+}:In_2O_3 NCs, a comprehensive analysis of the optical absorption spectra was conducted for all Co^{2+}:In_2O_3 NCs with varying Co concentrations. The strongest absorption feature represents the optical band gap of In_2O_3 NCs. Since In_2O_3 NCs display characteristics of direct band gap semiconductor, Tauc analysis was utilized to estimate their optical band gap energies. This estimation was performed by linear fitting of $(\alpha h\nu)^2$ against the photon energy ($h\nu$), as illustrated in the inset Figure 3.3.

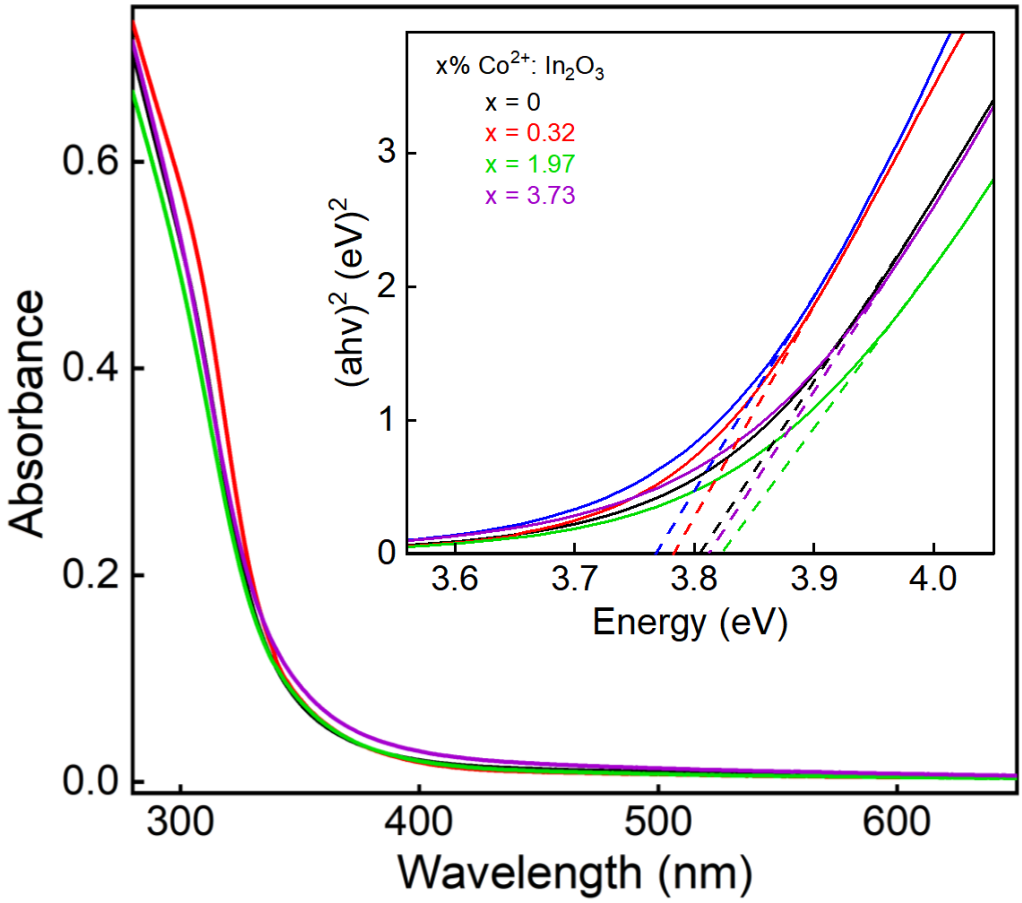

Figure 3.3 Optical absorption spectra of Co^{2+}:In_2O_3 NCs with varying Co doping concentrations. Inset shows the Tauc plot analysis for all NC samples indicating band gap energies corresponding to the intersection with the dash lines and Energy axis.

Based on the Tauc analysis, the band gap energies for all NC samples fall within a range from 3.77 eV to 3.83 eV, aligning closely with the literature-reported value of 3.75 eV. [19] Due to the relatively low Co concentration in Co^{2+}:In_2O_3 samples, the optical band gap energy does not exhibit any systematic shifts corresponding to the increase in Co concentration, as the Burstein-Moss effect observed in plasmonic semiconductor NC materials where the band gap widens with increased doping concentration.[69] This absence of a shift in the absorption spectra suggests that the doping levels used may not significantly alter the electronic structure of the

Co^{2+}:In_2O_3 NCs.

3.2.2 Optical Properties of the Effect of Co Dopants in Co^{2+}:In_2O_3 NCs

Indium oxide exhibits a cubic crystal structure, known as bixbyite-type or C-type rare-earth sesquioxide structure, with the space group $Ia\bar{3}$ (No. 206). The unit cell is composed of 16 formula units, with 32 cations and 48 anions. This structure adopts two non-equivalent six-coordinate In^{3+} sites, which are suitable for substitutional doping with Co^{2+} ions. These two sites, often referred to as *b* and *d* sites, have a distinctly different symmetry, with *d* site being more distorted. The *b* sites are more structured with the C_{3i} (or S_6) symmetry, while the *d* sites are highly distorted and adopt a C_2 point group symmetry.[52,54,55] Theoretical calculations and empirical evidence suggest that *d* site is preferentially occupied by the dopant ion when the dopant cation is smaller than In^{3+}, whereas *b* site is more favorable for dopants with effective ionic radii larger than In^{3+}.[55,58,61,70] Since Co^{2+} (74.5 pm)[71] is smaller than In^{3+} (80 pm)[71] in an octahedral configuration, we expect it to preferentially occupy the *d* site in bixbyite-type In_2O_3 structure.

Thus, to explore the optical absorption characteristics attributed to Co^{2+} dopants, the normalized absorption spectra of all Co^{2+}:In_2O_3 NCs with varying Co concentration were presented in Figure 3.4. For doping concentrations exceeding 1.97%, a series of weak transitions is observed between 500 nm and 700 nm. These spectral features can be assigned to spin-allowed ligand-field transitions of Co^{2+} in a six-coordinate environment. Even though these *d-d* transitions are formally forbidden by the Laporte selection rule, resulting in low intensities in an ideal octahedral environment, lowering the symmetry allows them to gain

additional intensity. In an ideal cubic octahedral symmetry with high-spin configuration, Co^{2+} with a ground state term symbol ^4F will split into $^4T_1$, $^4T_2$ and $^4A_2$ terms. Additionally, excited state ^4P atomic term gives rise to $^4T_1$ (P) state, as described in the inset of Figure 3.4. The dominant transition in oxo-coordinated Co^{2+} in the visible range is $^4T_1$ (F) → $^4T_1$ (P), which is typically split due to spin-orbit coupling[72,73] and an admixture of spin-forbidden transitions derived from ^2G and ^2H atomic terms. These spin-forbidden transitions to doublet states could also give rise to higher-energy absorption of octahedral Co^{2+}. Therefore, the structured absorption at wavelengths shorter than 600 nm (or energies above 16,700 cm^{-1}) is attributed to the $^4T_1$ (F) → $^4T_1$ (P) transition. Moreover, a spectral shoulder at around 620 nm may be assigned to $^4T_1$ → $^4A_2$ transition according to the inset in Figure 3.4.

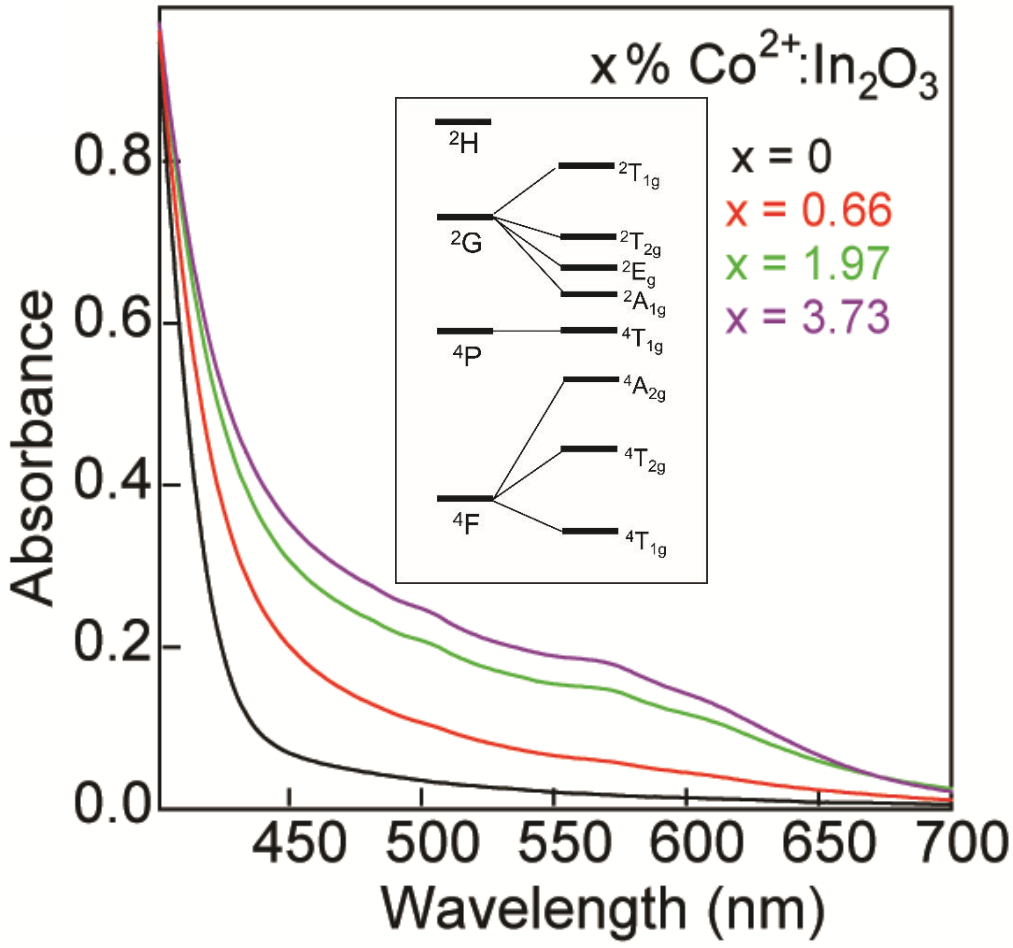

Figure 3.4 Normalized optical absorption spectra of Co^{2+}:In_2O_3 NCs with varying Co doping concentrations. Inset shows the splitting pattern for a Co^{2+} ion in a perfectly octahedral symmetry.

3.3 Magneto-Optical Properties of In_2O_3 and Co^{2+}:In_2O_3 NCs

3.3.1 Magneto-Optical Properties of Co^{2+}:In_2O_3 NCs in Co Transition Region

MCD spectroscopy measures the difference in absorption of LCP and RCP lights when an external magnetic field is applied parallel to the light propagation direction. It has been known that the MCD can be used to investigate the electronic structure of transition metal ions in crystal lattices and complexes. This is due to the sensitivity of MCD intensity to the spin-orbit coupling constant and the paramagnetism in the ground state (known as *C*-term MCD).[56,57] Therefore, to confirm the origin of absorption features related to Co^{2+} transitions as observed from the UV-Vis spectra, variable-field MCD measurements were performed on the series of Co^{2+}:In_2O_3 NCs with varying Co concentrations.

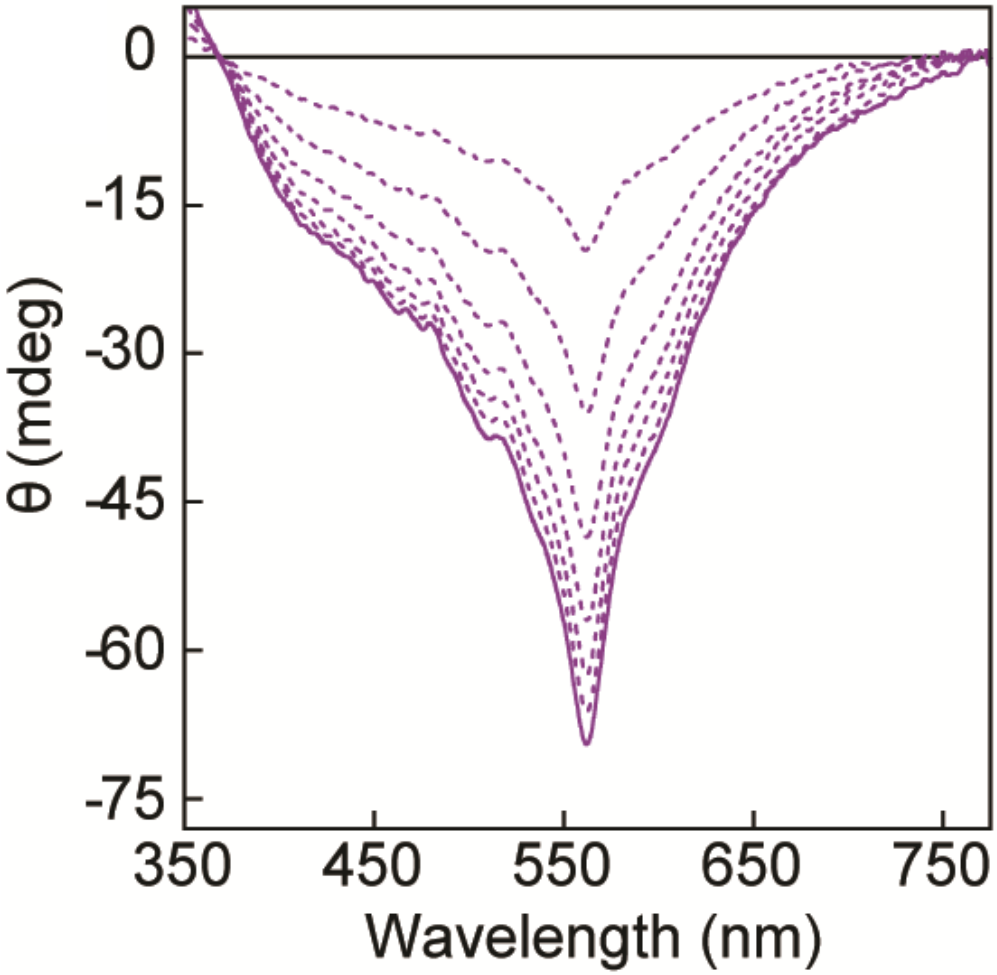

Figure 3.5 Field-dependent MCD spectra of 3.73% Co^{2+}:In_2O_3 NCs in the UV-Vis region. The MCD spectra were collected at 5 K with external magnetic fields ranging from 1 to 7 T.

Figure 3.5 shows the 5 K MCD spectra of typical Co^{2+}:In_2O_3 NCs collected in a variable magnetic field from 1 to 7 T. It is noted that the transitions seen in the electronic absorption spectra are considerably more pronounced at 5 K MCD spectra. Specifically, a distinct feature of the MCD spectra is a relatively sharp band at around 560 nm, consistent with Co^{2+}-related $^4T_1$ (F) → $^4T_1$ (P) transition. This is accompanied by a series of less intense bands at shorter wavelengths, which probably originated from the spin-forbidden transitions to doublet states. [72,73] Additionally, a set of broader and less defined spectral features, observed as shoulders tailing between ca. 600 and 750 nm, can be attributed to the components of $^4T_1$ → $^4A_2$ transition

for Co^{2+} dopants in In_2O_3 NCs.

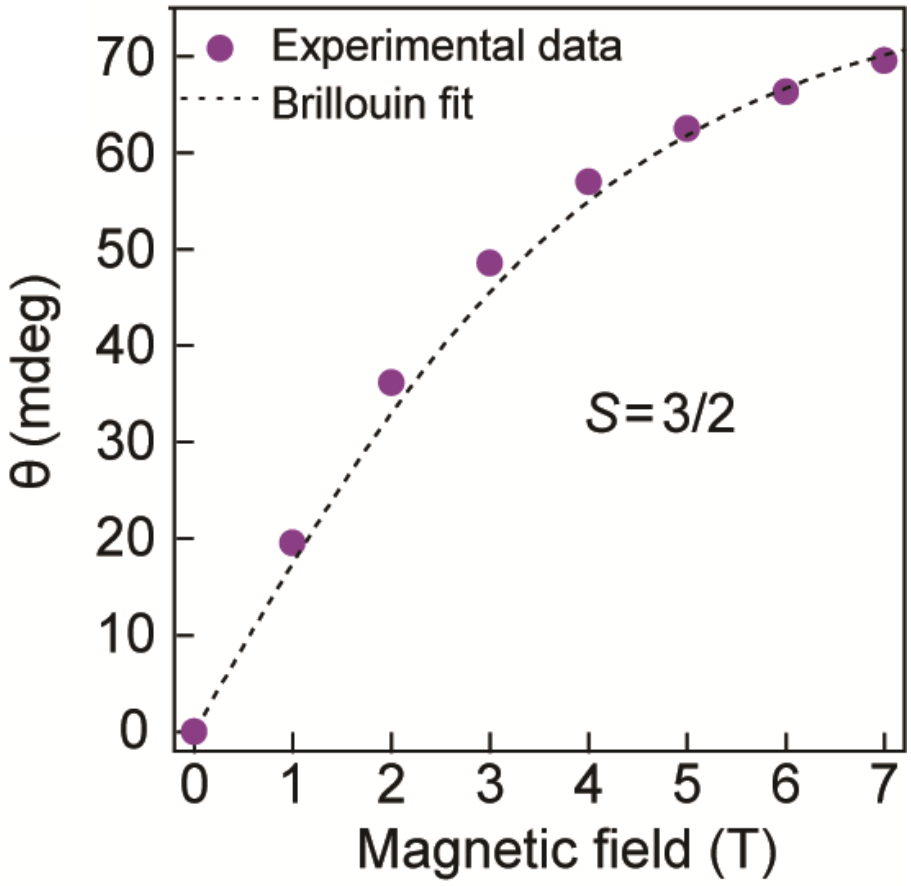

Figure 3.6 Field dependent MCD peak intensities at ca. 560 nm. The dash line is the Brillouin function fit to the experimental data with fixed *S* value indicated in the graph.

Importantly, the field-dependence of the monochromatic MCD intensities demonstrates a saturation trend at low temperature, a characteristic behavior for *C*-term MCD, as illustrated in Figure 3.6. To obtain deeper analysis, the Brillouin function was employed to fit the intensity data for further analysis. A good fit to the experimental data is achieved for fixed $g = 2.002$ (free electron *g* value for approximation) and $S = 3/2$ with *N* as the only fitting parameter. The specific spin state value $S = 3/2$ is characteristic of high-spin six-coordinate Co^{2+} ions, unambiguously confirming the origin of the absorption transitions in the visible range.

Additionally, similar spectra were observed for Co^{2+}:In_2O_3 NC samples whose surfaces are post-synthetically treated with TOPO, reinforcing the conclusion that Co^{2+} ions are readily substitutionally doped in In_2O_3 NC lattice during the synthesis.[28,61]

Additionally, there is another distinct band at 392 nm that has no corresponding peak in the absorption spectra. This band maintains a relatively constant MCD intensity with the increase in Co concentration. Figure 3.7 illustrates that even with a small amount of Co dopants substituted in the In_2O_3 host lattice (0.32%), this spectral feature at 392 nm can still be clearly observed, in contrast to the barely discernible Co^{2+} ligand field transitions at such low doping concentrations. However, compared to the case of Co^{2+}:In_2O_3 NCs with a higher Co concentration, especially the 3.73% sample (Figure 3.5), this band intensity is significantly lower than the Co^{2+} ligand field transition. Although the precise origin of this specific band is not fully understood, one possible hypothesis is that it may result from a charge transfer transition from the ligand O (2*p*) to Co^{2+} (3*d*) states. This type of transition has been observed in other transition metal ions in similar symmetry.[29,58,74]

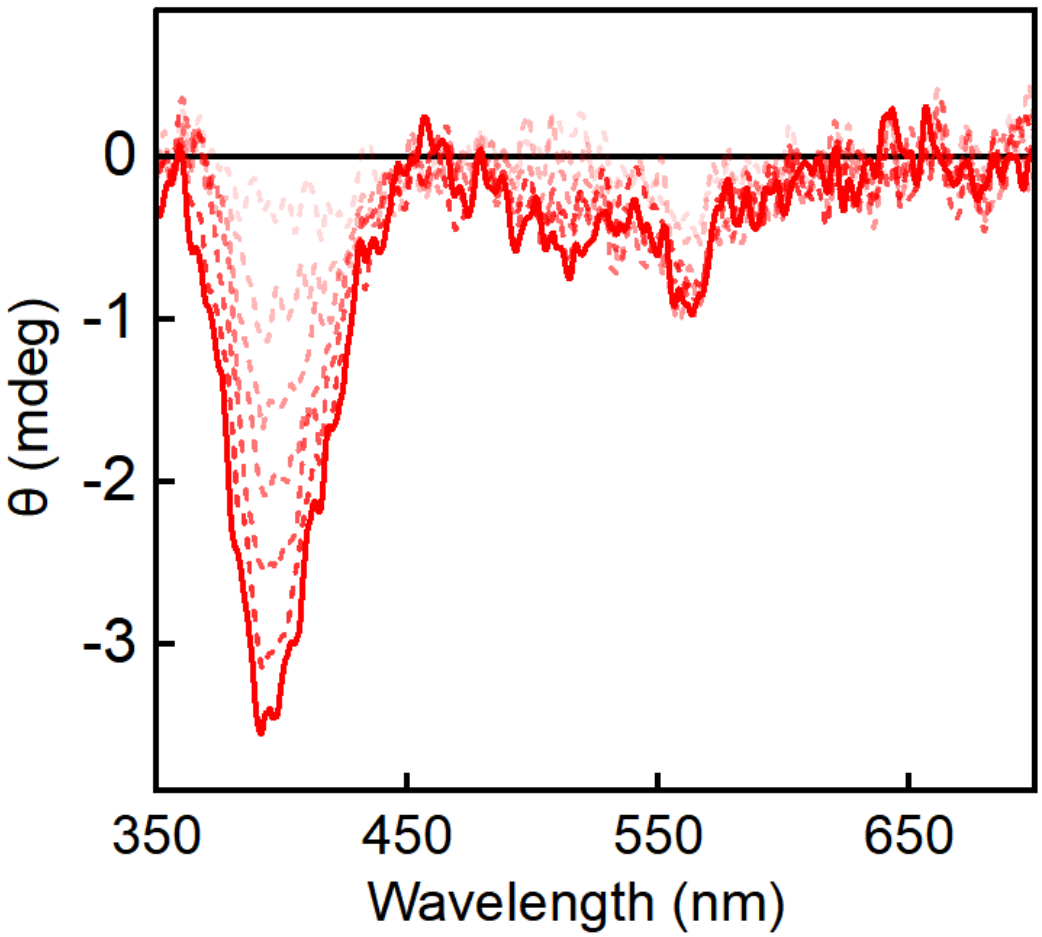

Figure 3.7 Field-dependent MCD spectra of 0.32% Co^{2+}:In_2O_3 NCs in the UV-Vis region. The MCD spectra were collected at 5 K with external magnetic fields ranging from 1 to 7 T.

3.3.2 Magneto-Optical Properties of Co^{2+}:In_2O_3 NCs in Excitonic Region

3.3.2.1 Field-Dependence of the MCD Spectra of Co^{2+}:In_2O_3 NCs in Excitonic Region

To investigate the spin exchange interactions between Co^{2+} dopant centers and NC band carriers in the In_2O_3 lattice and to understand the effect of Co^{2+} dopant incorporation on the magneto-optical properties of In_2O_3 NCs, MCD spectroscopy was conducted on Co^{2+}:In_2O_3 NCs with varying doping concentrations. A difference in the magneto-optical behavior may help reveal and deconvolute how the exchange interactions that polarize the excitonic states are manipulated through the transitional metal dopants and oxygen defects such as oxygen

vacancies.

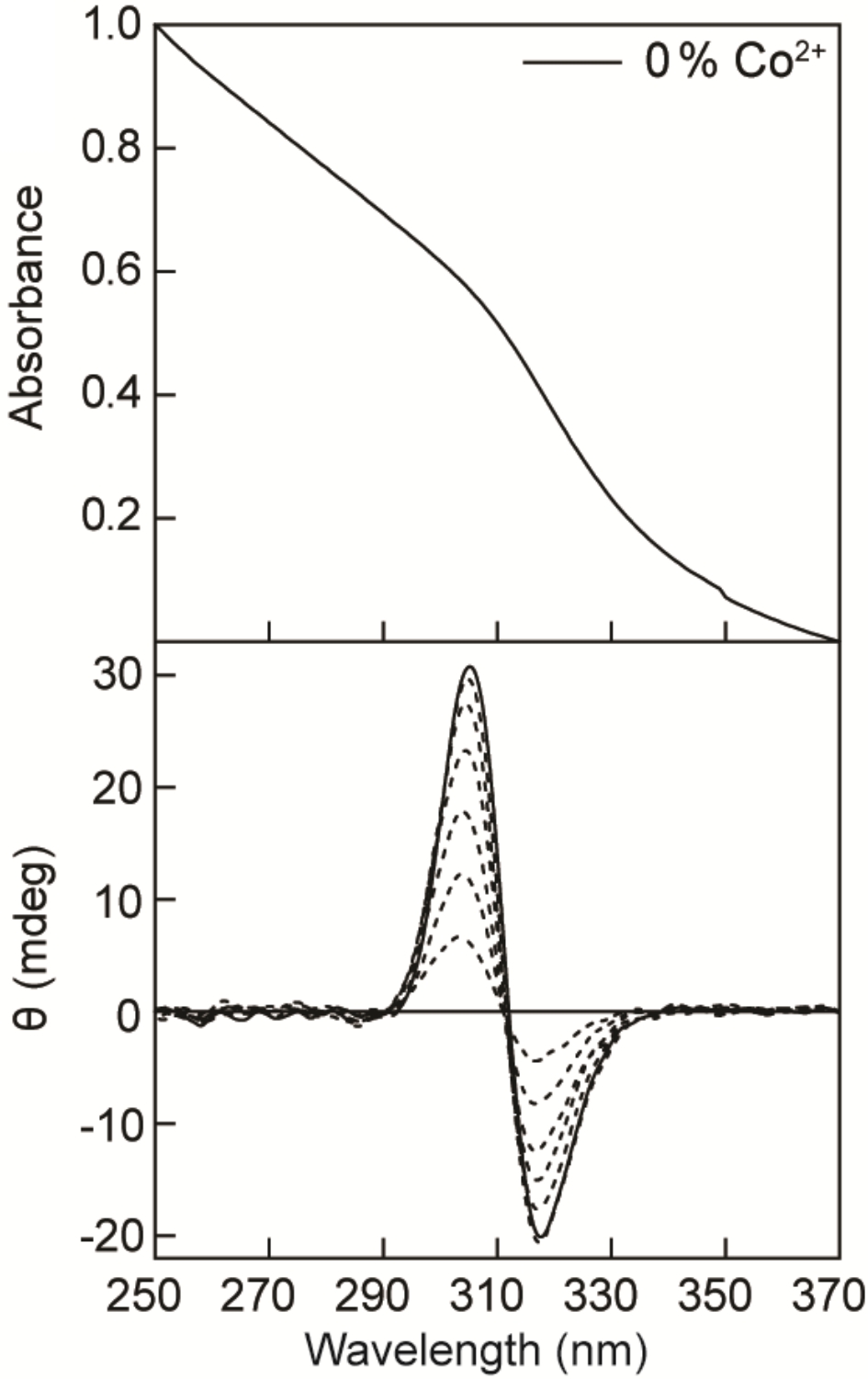

Figure 3.8 Optical absorption spectra (top panel) and MCD spectra (bottom panel) of undoped In_2O_3 NCs in the excitonic absorption region. The MCD spectra were collected at 5 K with

different external magnetic field strength from 1 to 7 T.

The MCD spectra of undoped In_2O_3 NCs were collected at 5 K with various magnetic field strengths ranging from 1 to 7 T, as shown in Figure 3.8 bottom panel. The undoped sample's MCD spectrum featured a pronounced derivative-shaped signal aligned with the excitonic transition energy observed in the optical absorption spectrum (Figure 3.8, top panel). The MCD signal saturates with increasing magnetic field strength, which is characteristic for a *C*-term contribution. This saturation suggests that the excitonic splitting arises from coupling of the NC band states with localized paramagnetic species arising from intrinsic point defects, such as the oxygen vacancies.

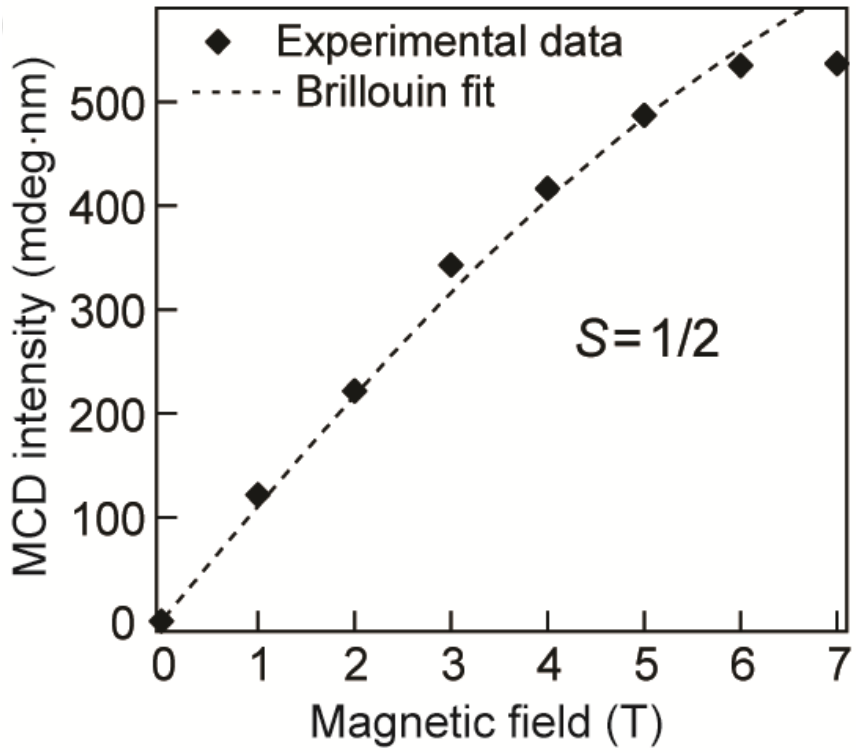

Figure 3.9 Magnetic field dependence of the integrated MCD intensity for undoped In_2O_3 NCs. The dash line is the Brillouin function fit to the experimental data with fixed *S* value indicated

in the graph. *N* is the only fitting parameter.

To identify the nature of the species responsible for inducing excitonic splitting in undoped In_2O_3 NCs, the MCD signal intensities were integrated, and the data points were fitted with the Brillouin function. As shown in Figure 3.9, a good fit to the experimental data is achieved up to 6 T for g = 2.002 as the free electron Lande g value and S = 1/2 as the spin-state of the paramagnetic centers, with density of the magnetic centers (N) as the only fitting parameter. This fitting indicates that these paramagnetic species contain one unpaired electron, strongly suggesting that the singly charged oxygen vacancies ($V_o^{\cdot}$) might be responsible for splitting of the excitonic states. Thus, the repercussion of these results is that these native defects in undoped In_2O_3 are capable of inducing DMS-like behavior even without the incorporation of transition metal dopants, which is consistent with previous studies on transparent metal oxide NCs prepared under similar conditions.[24,75,76]

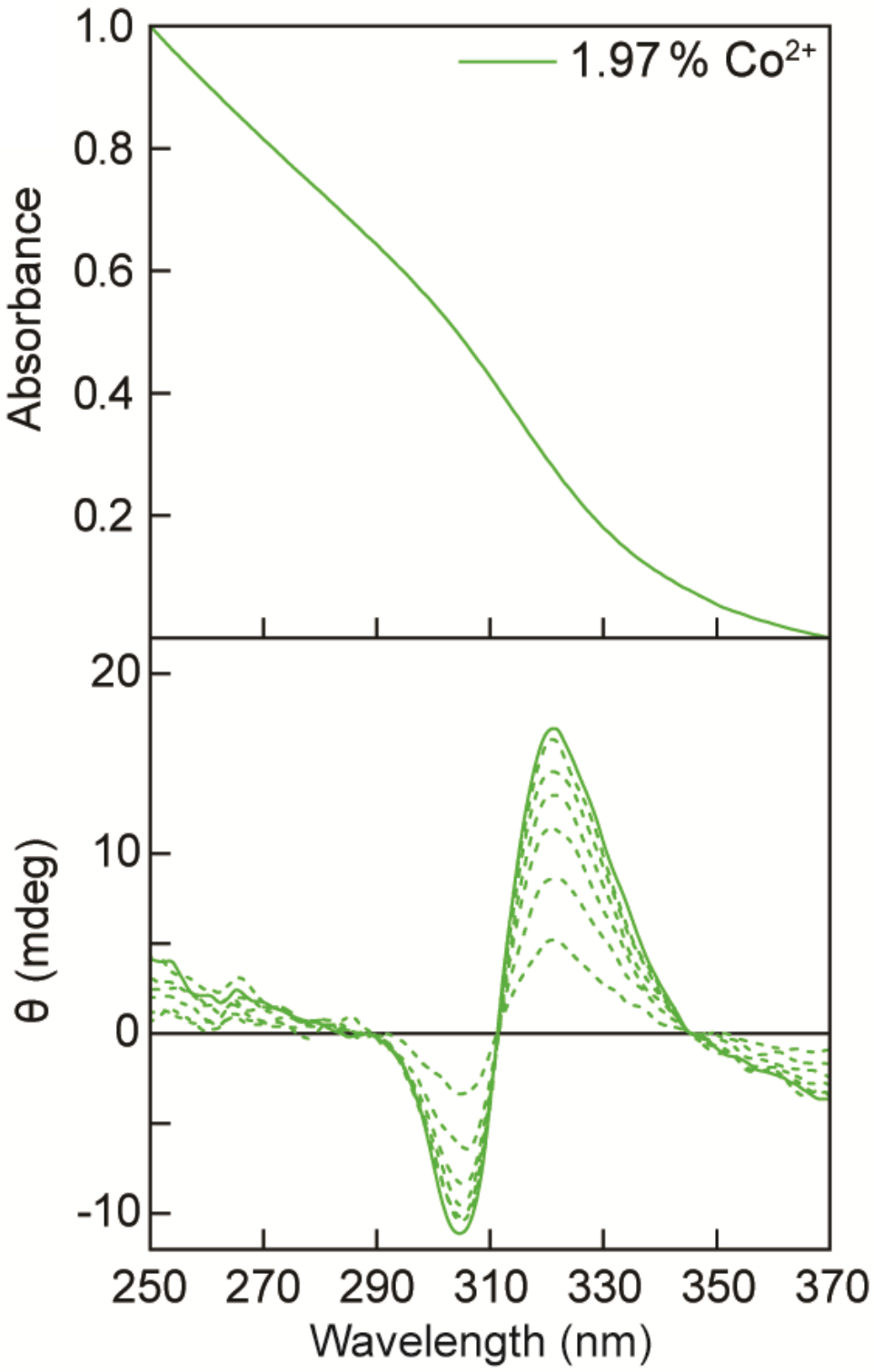

Figure 3.10 The optical absorption spectra (top panel) and MCD spectra (bottom panel) of 1.97% Co^{2+}:In_2O_3 NCs in the excitonic absorption region. The MCD spectra were collected at 5 K with different external magnetic field strength from 1 to 7 T.

The field-dependence of MCD spectra of 1.97% Co^{2+}:In_2O_3 NCs (bottom panel) and corresponding absorption spectrum (top panel) are presented in Figure 3.10. With the increasing concentration of Co dopants, it is noted that even though an excitonic splitting corresponding to the band gap absorption of In_2O_3 still persists, the sign of the bands has reversed. This inversion indicates that the localized d electrons of Co^{2+} ions result in a robust excitonic MCD signal with a polarity opposite to the splitting induced by singly-charged oxygen vacancies in undoped In_2O_3 NCs. Broadening of the excitonic band could be attributed to a higher polydispersity in average NC diameter for Co^{2+}:In_2O_3 NCs with high Co concentration relative to undoped In_2O_3 NCs.

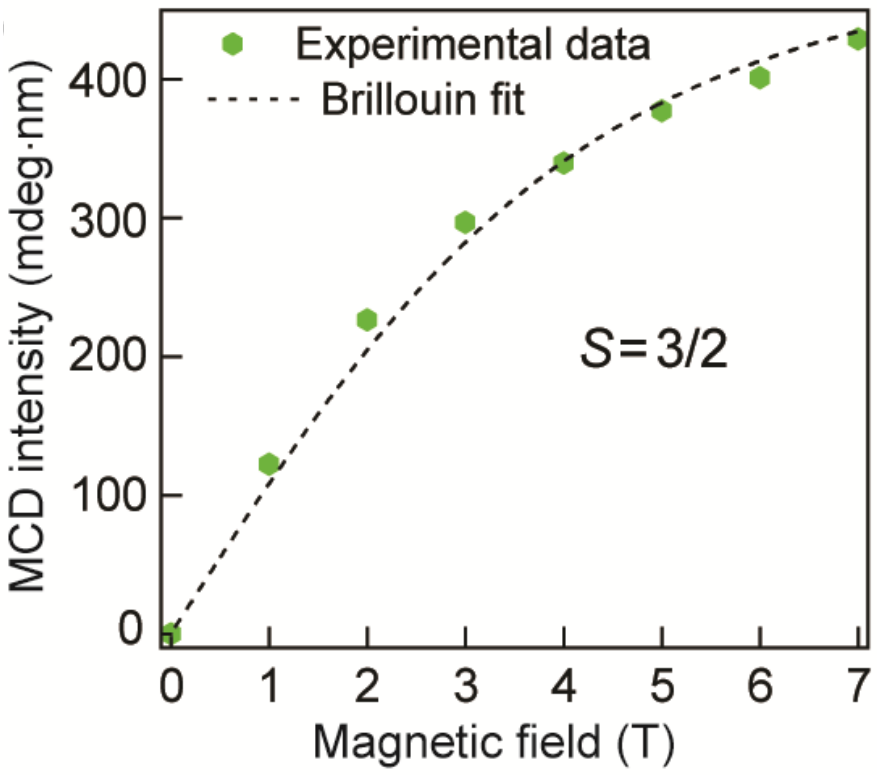

Figure 3.11 Magnetic field dependence of the integrated MCD intensity for 1.97% Co^{2+}:In_2O_3 NCs. The dash line is the Brillouin function fit to the experimental data with fixed *S* value indicated in the graph. *N* is the only fitting parameter.

Furthermore, the MCD signal of 1.97% Co^{2+}:In_2O_3 NCs saturates at a higher rate with an increasing magnetic field strength compared to the undoped sample. As observed in Figure 3.10, an excellent Brillouin function fit to the field-dependence of the integrated excitonic MCD intensity is achieved for S = 3/2, which is in prefect agreement with the Co^{2+} ligand-field transitions in Figure 3.6. This agreement unambiguously proves that Co^{2+} dopants cause anomalous Zeeman splitting of In_2O_3 NC band states, resulting in the true DMS behavior.

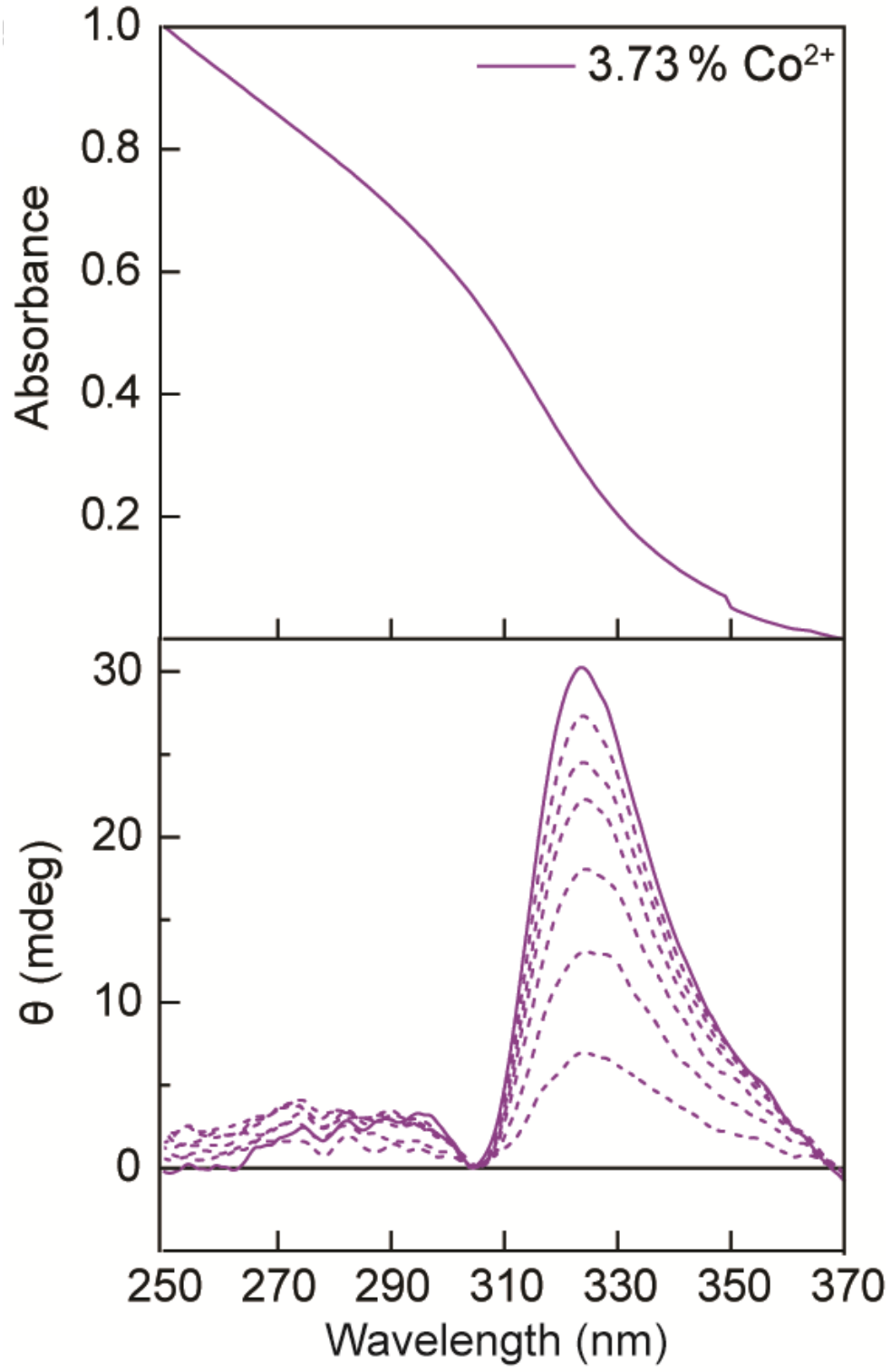

Figure 3.12 The optical absorption spectra (top panel) and MCD spectra (bottom panel) of 3.73% Co^{2+}:In_2O_3 NCs in the excitonic absorption region. The MCD spectra were collected at 5 K with different external magnetic field strength from 1 to 7 T.

To further investigate the effect of dopant concentration on the excitonic splitting in the In_2O_3 lattice, I performed the MCD measurements on Co^{2+}:In_2O_3 NCs with higher Co concentration. According to Figure 3.12, the excitonic MCD spectra of 3.73% Co^{2+}:In_2O_3 NCs has a typical *C*-term character, demonstrating a completely polarized excitonic population with only a positive (absorption-like) band and no related negative band. The positive band bears an asymmetric band shape as compared to a symmetric signal from undoped In_2O_3 NCs and is consistent with the coupling of excitonic states with other transition metal ions as reported in previous studies.[58,74]

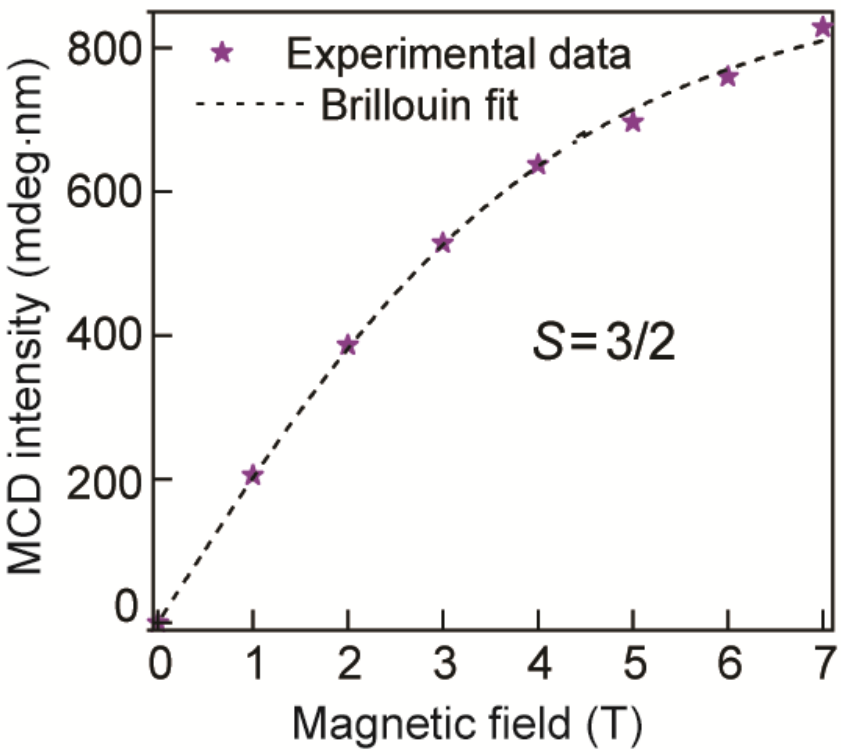

Figure 3.13 Magnetic field dependence of the integrated MCD intensities of the positive band for 3.73% Co^{2+}:In_2O_3 NCs. The dash line is the Brillouin function fit to the experimental data with fixed *S* value indicated in the graph. *N* is the only fitting parameter.

As shown in Figure 3.13, the integrated MCD intensities were fitted to a spin-only

Brillouin function corresponding to the spin-state value of 3/2, which is equivalent to the expected value for an exciton coupled to Co^{2+} ions in the In_2O_3 lattice. Therefore, we could drastically manipulate the extent of polarization of exciton in the In_2O_3 lattice, which is fundamentally driven by change in the dominant contribution to Zeeman splitting, from either intrinsic defects of extrinsic dopants.

Taken together, these results for Co^{2+}:In_2O_3 NCs with varying Co^{2+} concentrations indicate that Zeeman splitting induced by transition metal dopants competes with the splitting induced by localized spins on native defect sites. This competition potentially allows for tuning the exciton splitting pattern and magneto-optical properties of DMSO NCs by controlling the dominant source of spin exchange coupling.

3.3.2.2 Normalized MCD Spectra of Co^{2+}:In_2O_3 NCs in Excitonic Region

Figure 3.14 plots the normalized MCD spectra of Co^{2+}:In_2O_3 NCs with different doping concentrations, obtained by converting ellipticity (θ) to $\Delta A/A$ using Equation 2.3. This comparison provides a comprehensive analysis to infer the effect of Co^{2+} doping on the degree of excitonic Zeeman splitting. The normalized plot reveals that by introducing a small amount of Co dopants (0.32%), the intensity of the MCD band is significantly suppressed compared to undoped In_2O_3 NCs with only intrinsic defects, although the sign of the MCD signal remains unchanged.

Increase in Co^{2+} doping concentration (1.97 %) flips the sign of the MCD signal, which is an indication that the mechanism governing the Zeeman splitting of the excitonic states has changed. Surprisingly, the integrated $\Delta A/A$ intensity does not exhibit significant differences

between undoped and Co^{2+}-doped In_2O_3 samples. This observation indicates that the Zeeman splitting energies remain comparable across these samples, which leads to anomalous dependence of the MCD signal intensity on doping concentration. Based on the normalized MCD spectra, as the concentration of Co^{2+} dopant increases, the effective Zeeman splitting initially decreases and is completely cancelled for doping concentrations of around 0.5%.

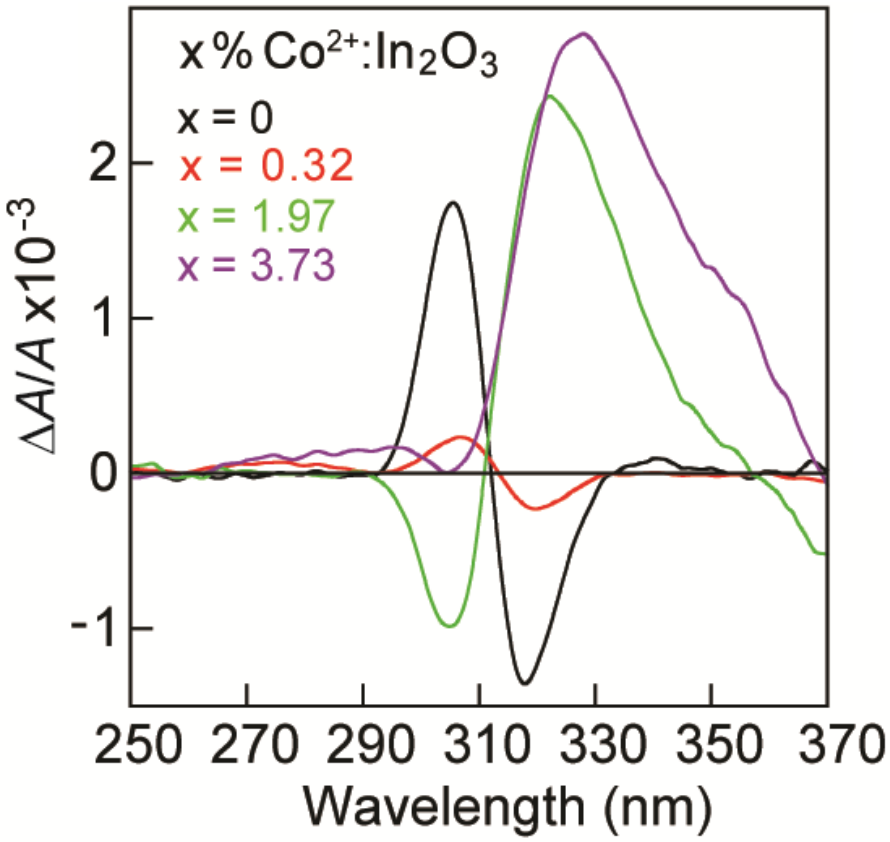

Figure 3.14 The normalized MCD spectra of Co^{2+}:In_2O_3 NCs in the excitonic absorption region. All spectra were collected at 5 K under 7 T and converted to ΔA/A by dividing with the corresponding absorbance in the same range.

With further increase in the Co^{2+} dopant concentration (3.73%), the negative band of MCD signal disappears, while the positive band remains mostly unchanged, suggesting a change in the electronic structure of the NCs. This can be corroborated by the observation that the

Brillouin fit to the integrated MCD signal for 3.73% Co^{2+}:In_2O_3 NCs is in excellent agreement with $S = 3/2$ (indicated in the Figure 3.13), which is the expected spin-state for Co^{2+} ions in a high-spin octahedral d^7 electronic configuration.

While the theory of Zeeman splitting of the band structure of DMSs based on II-VI and III-V semiconductors has been well developed,[4,11] general models applicable to other DMSs are still lacking. In wurtzite lattices, characteristic for II-VI and III-V semiconductors, the excitonic Zeeman splitting is governed by *sp-d* exchange interactions. These interactions are described by $N_0\alpha$ (*s-d*) and $N_0\beta$ (*p-d*) coupling constants. The sign and magnitude of these constants determine the polarization of the electronic band charge carriers in the host lattice,[4] with $N_0\beta$ being the dominant component due to hybridization of the wavefunctions of *p*-band (valence band) and dopant *d*-electrons. While the theoretical framework for In_2O_3-based DMSs has not been established, some important quantitative conclusions can be drawn from our results.

To that end, it is important to first understand what causes this change in the polarization of the exciton population as the Co doping percentage has increased. Firstly, it is apparent that an increase in the Co^{2+} doping concentration increases the spin exchange interactions, which leads to the polarization of excitonic states. On the other hand, the intrinsic contribution to the MCD signal is not constant for different Co^{2+}:In_2O_3 NCs. With an increase in the Co^{2+} doping concentration the average diameter of the NCs decreases. This affects the concentration of oxygen vacancies, which are formed more favorably in the vicinity of NC surfaces.[75,77] Furthermore, the equilibrium concentration of oxygen vacancies and their charging are also affected by the doping concentration, irrespective of the change in NC size.[28,54,75,78] Another reasons for the influence of the dopant ions on the formation and distribution of oxygen

vacancies is electrostatic interaction, whereby point defects with a positive net charge (such as $V_O^{\cdot}$) are attracted to those with a negative net charge (e.g., a Co^{2+} ion at a In^{3+} site).[79,80] While oxygen vacancies at the NC surface do not exhibit significant exchange interactions with the excitonic states,[75] the internal vacancies should lead to an increase in the intrinsic MCD signal with increasing doping concentration. Given that the excitonic MCD signal related to Co^{2+} dopants (S = 3/2) saturates much faster than that related to oxygen vacancies (S = 1/2), introduction of a certain amount of Co^{2+} is needed to overcome the intrinsic exciton polarization induced by native defects. Further increase in Co^{2+} doping level increases the exciton polarization through the kinetic exchange mechanism. However, the results of Figure 3.14 suggest that, in contrast to II-VI DMS quantum dots,[81] in case of Co^{2+}:In_2O_3 NCs intrinsic Zeeman splitting is comparable to the Zeeman splitting induced by transition metal dopant centers, owing to the different origin of the intrinsic contributions. This competition between the intrinsic and dopant-related exciton polarization results in an anomalous magneto-optical behavior of Co^{2+}:In_2O_3 NCs with respect to the doping concentration, as observed in Figure 3.14.

3.3.2.3 Excitonic Zeeman Splitting Energy Calculation

To conduct a quantitative analysis and compare Co^{2+}:In_2O_3 NCs with varying Co concentrations, the energy of excitonic Zeeman splitting (ΔE_Z) can be calculated through the equation 2.4.[64] Based on this equation, the Zeeman splitting energy and its field dependence for all samples can be estimated from the absorption and MCD spectra. This calculation allows for a detailed investigation into the effects and contributions of both intrinsic defects and extrinsic dopants on excitonic Zeeman splitting.

Co^{2+} doping concentration (%)	Zeeman's Splitting Energy High Energy Band (meV)	Zeeman's Splitting Energy Low Energy Band (meV)	Average Zeeman's Splitting Energy (meV)
0	0.2534	0.1593	0.2064
0.32	0.0308	0.0317	0.0313
1.97	0.1532	0.3703	0.2618
3.73	-NA-	0.6595	0.6595

Table 3.2 Summary of estimated Zeeman's splitting energy for Co^{2+}:In_2O_3 NCs with varying Co concentration.

Since the MCD spectra of Co^{2+}:In_2O_3 NCs exhibit asymmetric peaks, particularly for higher doping concentrations, we used the lower energy peak to calculate the Zeeman splitting energy because it is consistently present for every sample. For comparison, Table 3.2 provides the values of the Zeeman splitting energy using the higher energy peak and an average value of the higher and lower energy peaks.

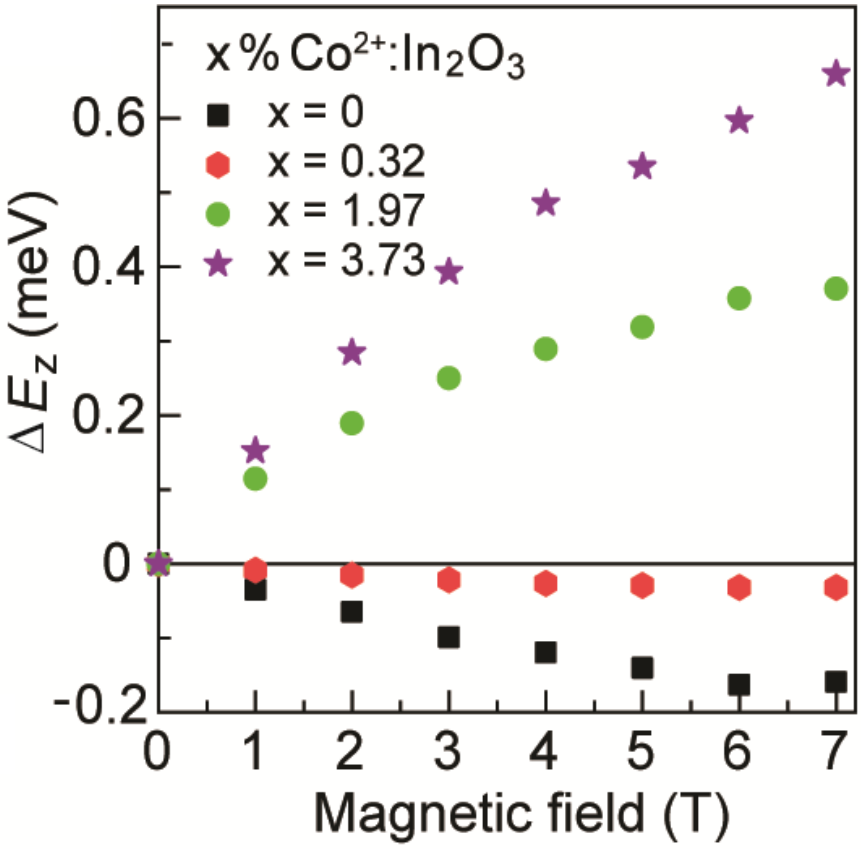

Figure 3.15 Estimated Zeeman's splitting energy for different magnetic field strength for various Co^{2+}:In_2O_3 NCs.

The magnetic field dependence of ΔE_Z for undoped and Co^{2+}-doped In_2O_3 NCs are shown in Figure 3.15. As an example, ΔE_Z value for undoped In_2O_3 at 7 T is almost 60 % of the Zeeman splitting energy for 1.97 % Co^{2+}:In_2O_3 NCs, confirming that intrinsic contributions cannot be ignored in metal oxide NCs.

	Sample	Average NC diameter (nm)	Volume of NC (nm^3)	Number of dopants per NC	ΔE_z (meV)
Actual	0 % Co	8.9	369.1	0	0.1593
	0.32 % Co	6.5	143.8	14.4	0.0318
	1.97 % Co	5.2	73.6	45.2	0.3703
	3.73 % Co	5.6	91.9	108.2	0.6595
Normalized	0 % Co	5.1	69.5	0	0.0299
	0.32 % Co	5.1	69.5	6.97	0.0153
	1.97 % Co	5.1	69.5	42.7	0.3493
	3.73 % Co	5.1	69.5	81.7	0.4982
Hypothesis	0.54 % Co	5.1	69.5	12	0
Comparison	0.003 % Mn:CdSe	5.1	69.5	1	~0.4

Table 3.3 A comparison of Zeeman's splitting energy (ΔE_Z) of Co^{2+}:In_2O_3 NCs with literature and size normalized hypothetical samples with the same composition to estimate the strength of *sp-d* exchange interactions across different systems. Mn^{2+}-doped CdSe (Mn:CdSe) NCs obtained from reference data has been listed for comparison.[64]

As shown in Table 3.3, another important quantitative comparison that could be established is the number of Co^{2+} dopants required to quench the intrinsic excitonic signal originated from the oxygen defects in In_2O_3 NCs. At 0.32 % Co^{2+} doping concentration, the intrinsic excitonic signal is almost quenched (Figure 3.14). These NCs have an average diameter of 10.8 nm, and therefore contain over 60 Co^{2+} ions. Comparing that with a typical II-VI semiconductor DMS NC system, such as Mn^{2+}-doped CdSe, only 1 Mn^{2+} ion is sufficient to overcome the intrinsic exciton polarization in 5.1 nm NCs. For a fair comparison, if we normalize the effect of NC volume, a 5.1 nm 0.32 % Co^{2+}:In_2O_3 NC would have ~7 dopant ions. Furthermore, plotting the variation of ΔE_Z with respect to Co^{2+} doping percentage allows us to extract the doping percentage for which the effects of native defect and dopants cancel out (Figure 3.16 left panel). At low doping concentrations where inter-dopant interactions can be ignored, *sp-d* exchange interactions scale almost linearly with dopant concentration. Linear fit

to the data in Figure 3.16 left panel reveals that ca. 0.54 % Co^{2+} (or ~12 Co^{2+} per NC for a 5.1 nm NC) would be required to overcome the intrinsic effect, which is an order of magnitude more than for Mn^{2+}-doped CdSe NCs having the same size.

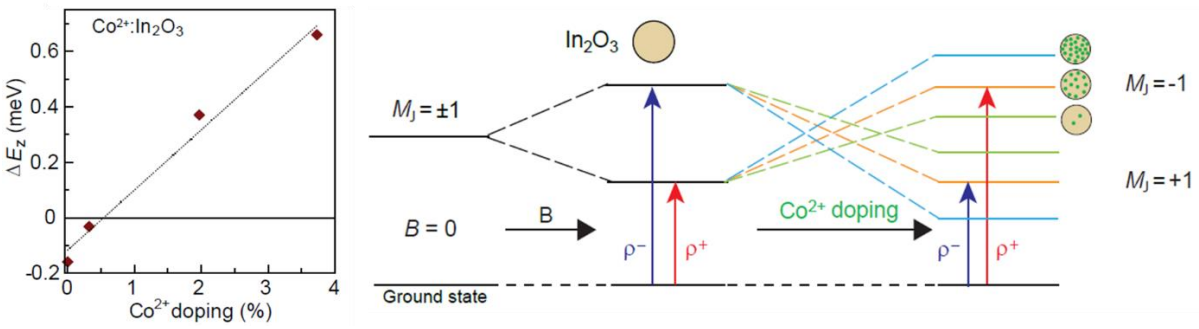

Figure 3.16 Variation of Zeeman splitting energy at 5 K, 7T with Co^{2+} doping percentage in Co^{2+}:In_2O_3 NCs (left), and schematic representation of the mechanism of exciton polarization with increasing Co^{2+} doping in In_2O_3 lattice (right).

3.4 Conclusion

In conclusion, I synthesized a series of Co^{2+}:In_2O_3 NCs with varying doping concentrations and investigated their magneto-optical properties using MCD spectroscopy. We compared the MCD spectra of undoped In_2O_3 and Co^{2+}:In_2O_3 NCs, and investigated the evolution of exciton polarization for increasing Co^{2+} doping concentration. The spectroscopic results reveal that band splitting in undoped and lightly-doped NCs is dominated by exchange interactions involving singly-charged oxygen vacancies in the presence of an applied magnetic field. With increasing Co^{2+} doping level, the dopant-induced exchange interactions take over as the dominant mechanism governing the anomalous Zeeman splitting of the NC band states. Surprisingly, the two types of exchange interactions are found to be comparable in magnitude

but result in the opposite splitting pattern of the band states. This competition between the two contributions leads to an anomalous behavior, including the cancelation of the MCD signal for Co^{2+} doping concentration of ca. 0.5 % (~12 dopants per 5 nm diameter NC). Results of this work demonstrate why it is so difficult to predict and consistently reproduce the behavior of DMSOs and consideration of these contributions would allow to better design the systems for spintronics and quantum information processing technologies.

Chapter 4

Study of Structural and Magneto-optical Properties in Shell-doped Cobalt-Doped Indium Oxide Nanocrystals

In this chapter of the thesis, I present a modified slow-injection synthesis method for preparing the Co^{2+}:In_2O_3 core/shell NCs. The successful formation of these core/shell NCs is corroborated through various structural analysis methods, including XRD, TEM, and ICP-OES characterizations. To further investigate how the Co^{2+} dopant location and NC sizes influence the magneto-optical properties of these NCs, I prepared two specific types of core-shell NCs: one with the Co^{2+} dopants incorporated into the core and the other with Co^{2+} dopants substituted into the NC shell. The comparison of the excitonic MCD spectra between the core- and shell-doped samples demonstrated that the strength of exchange interactions induced by Co^{2+} dopants remain relatively consistent regardless of the radial dopant position for larger NCs. However, the excitonic MCD intensity is nearly an order of magnitude larger for uniformly doped NCs, which suggests that the smaller size NCs comparable to Bohr radius leads to a much stronger dopant-exciton coupling, resulting in a larger dopant-induced excitonic Zeeman splitting.

4.1 Structural Characterization of Core/Shell Co^{2+}:In_2O_3 NCs

4.1.1 Crystal structure of Core/Shell Co^{2+}:In_2O_3 NCs

The synthesis of colloidal core/shell configuration Co^{2+}:In_2O_3 NCs with Co^{2+} presence either in the core or on the shell was performed by a slow-injection method using standard Schlenk line techniques, detailed in the Experimental Section 2.2.3. [58,61] While core-shell heterostructures for metal oxide NCs have been designed previously,[82,83] the incorporation of

transition metal dopants through this approach has not been reported before.

For the core- and shell-doped sample, 5 atomic % of Co^{2+} precursor relative to In^{3+} precursor was introduced during the core formation and shell growth of Co^{2+}:In_2O_3 NCs, resoectively, resulting in an estimated ca. 2% overall theoretical doping concentration within the core/shell structure.

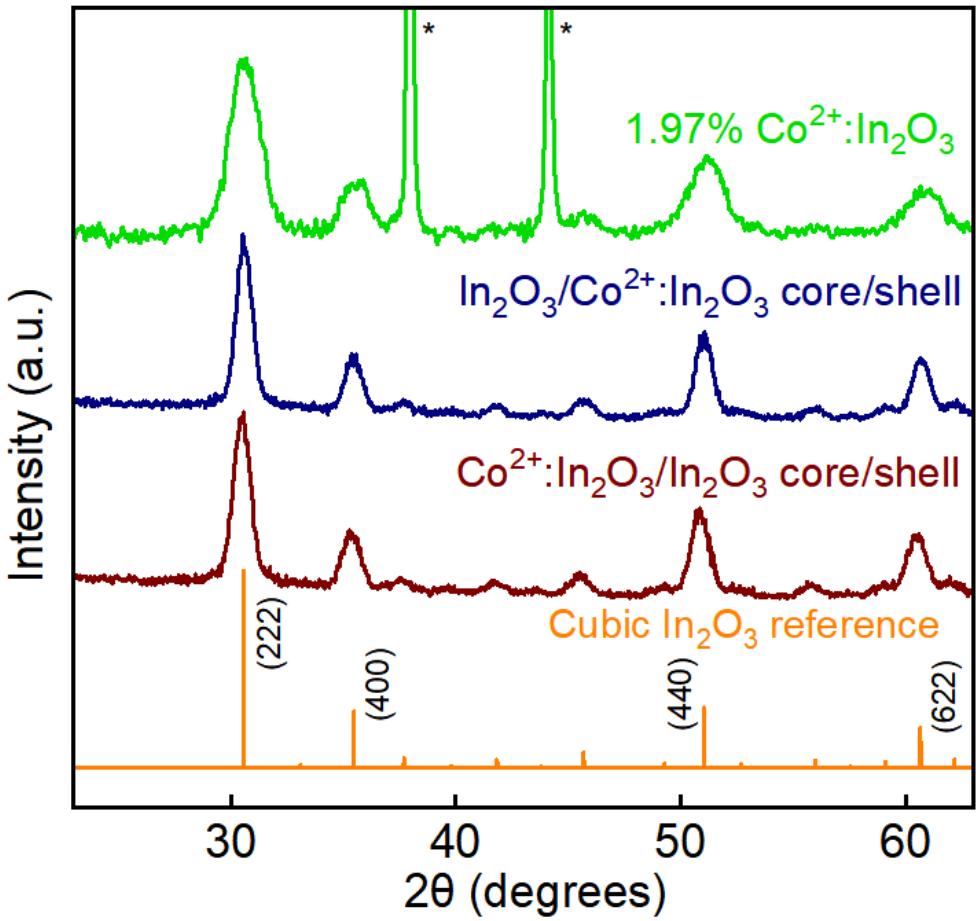

Figure 4.1 Powder XRD pattern of core doped (brown trace) and shell-doped (blue trace) Co^{2+}:In_2O_3 NCs. Two sharp peaks marked with * represent the Al substrate. The green XRD pattern is the 1.97 % uniformly-doped Co^{2+}:In_2O_3 sample prepared according to Experiment Section 2.2.2. The orange vertical lines correspond to the reference XRD pattern of cubic bixbyite In_2O_3 (JCPDS No.88-2160).

The powder XRD patterns were collected to determine the crystal structure of the as-synthesized core/shell structure Co^{2+}:In_2O_3 NC samples. As displayed in Figure 4.1, the XRD patterns of both core-doped and shell-doped Co^{2+}:In_2O_3 NCs corresponds to the reference pattern of bulk cubic-phase In_2O_3 (indicated by orange vertical lines, JCPDS No.88-2160). This agreement confirms that the both core-doped and shell-doped Co^{2+}:In_2O_3 NCs exhibit high purity body-centered cubic structure without any secondary phase observed.

Furthermore, as illustrated in Figure 4.1, the shape of XRD peaks for the core/shell Co^{2+}:In_2O_3 NCs are comparable to each other, but appear noticeably sharper than those for uniformly-doped sample with a similar overall doping concentration (1.97 %) discussed in the previous chapter. This enhanced sharpness in the XRD peaks indicates that the core/shell-structured NCs exhibit a larger average size compared to the uniformly doped samples. Based on the Scherrer equation analysis, the average size of both core/shell Co^{2+}:In_2O_3 NC samples have been calculated to be approximately 11 nm, which is significantly larger than the uniformly-doped sample.

4.1.2 Elemental Analysis of Core/Shell Co^{2+}:In_2O_3 NCs

The actual dopant concentration in the core/shell-structured sample was accurately quantified through ICP-OES. The analysis revealed that the actual concentration of Co dopants for core-doped and shell-doped samples are approximately 1.85% and 2.03 %, respectively. Notably, these measured concentrations closely align with the precursor ratios employed in the synthesis process, resulting in about half of the nominal concentration intended for the shell. This agreement of measured concentration indicates the effectiveness of the shell growth

process, and confirms the successful incorporation of Co^{2+} ions into the In_2O_3 NCs during the synthesis.

4.1.3 Morphology Study of Core/Shell Co^{2+}:In_2O_3 NCs

To study the morphology of the core/shell Co^{2+}:In_2O_3 NCs and confirm the successful completion of the shell-growth step, the TEM imaging was performed for the core- and shell-doped Co^{2+}:In_2O_3 samples in both the core and the corresponding core/shell structures. The TEM images shown in Figure 4.2 provide an overview of the NC cores and core/shell structures for both samples.

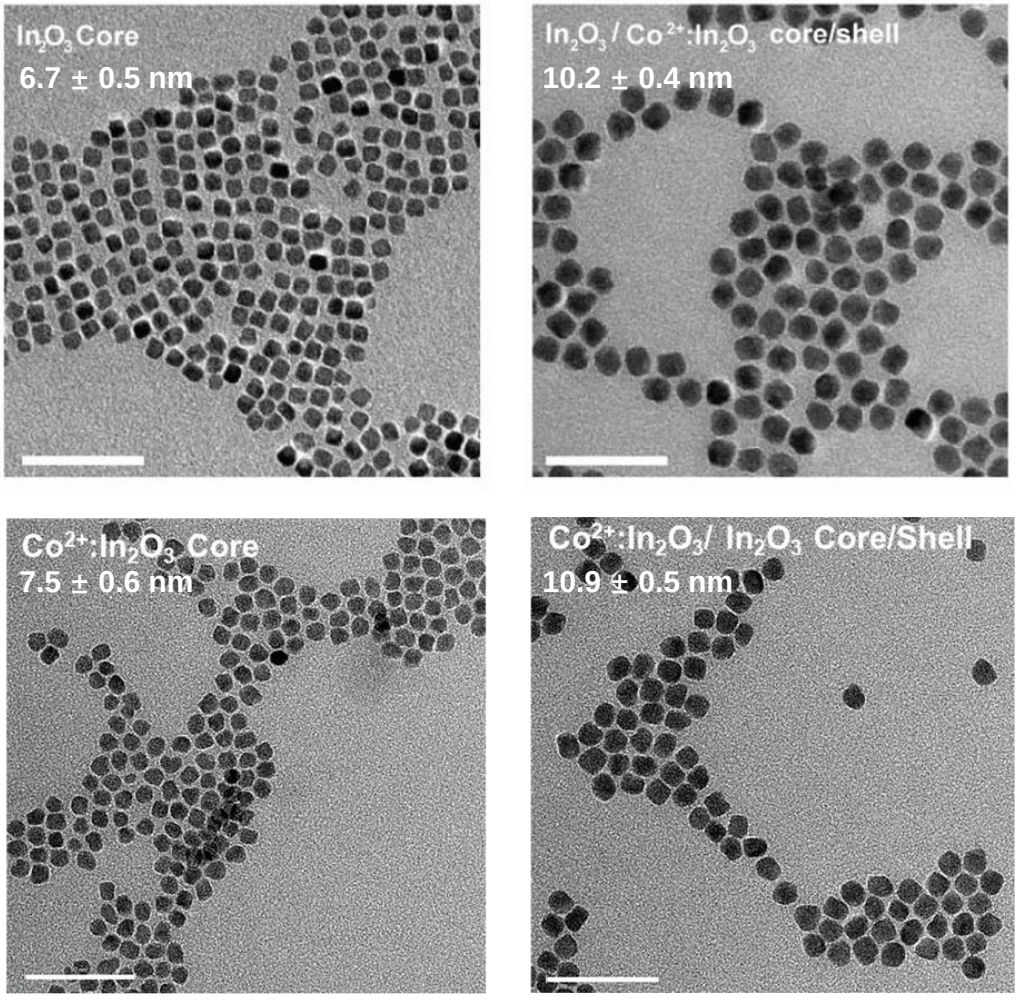

Figure 4.2 The TEM images of shell-doped (top) and core-doped (bottom) Co^{2+}:In_2O_3 NCs

with both NC cores (left) and corresponding core/shell NC configurations (right) indicated in the figure. The average NC sizes are also shown as insets. All scale bars are 50 nm.

From Figure 4.2, most NCs adopt the quasi-spherical or square shape with a relatively uniform size distribution. A comparative analysis of the average NC sizes of shell-doped Co^{2+}:In_2O_3 NCs indicates a remarkable increase in the overall size of NC after the growth of the shell (from 6.7 ± 0.5 nm to 10.2 ± 0.4 nm). The average thickness of the shell is estimated to be ~ 1.7 nm and the total NC radius ~ 5.1 nm, confirming that most of the dopants are indeed present relatively close to the surface of the NCs.Similarly, the core-doped Co^{2+}:In_2O_3 NCs have an average core diameter of 7.5 nm and shell thickness of 1.7 nm. The significant increases in average size confirm the successful formation of the core/shell configuration in both core-doped and shell-doped Co^{2+}:In_2O_3 NCs.

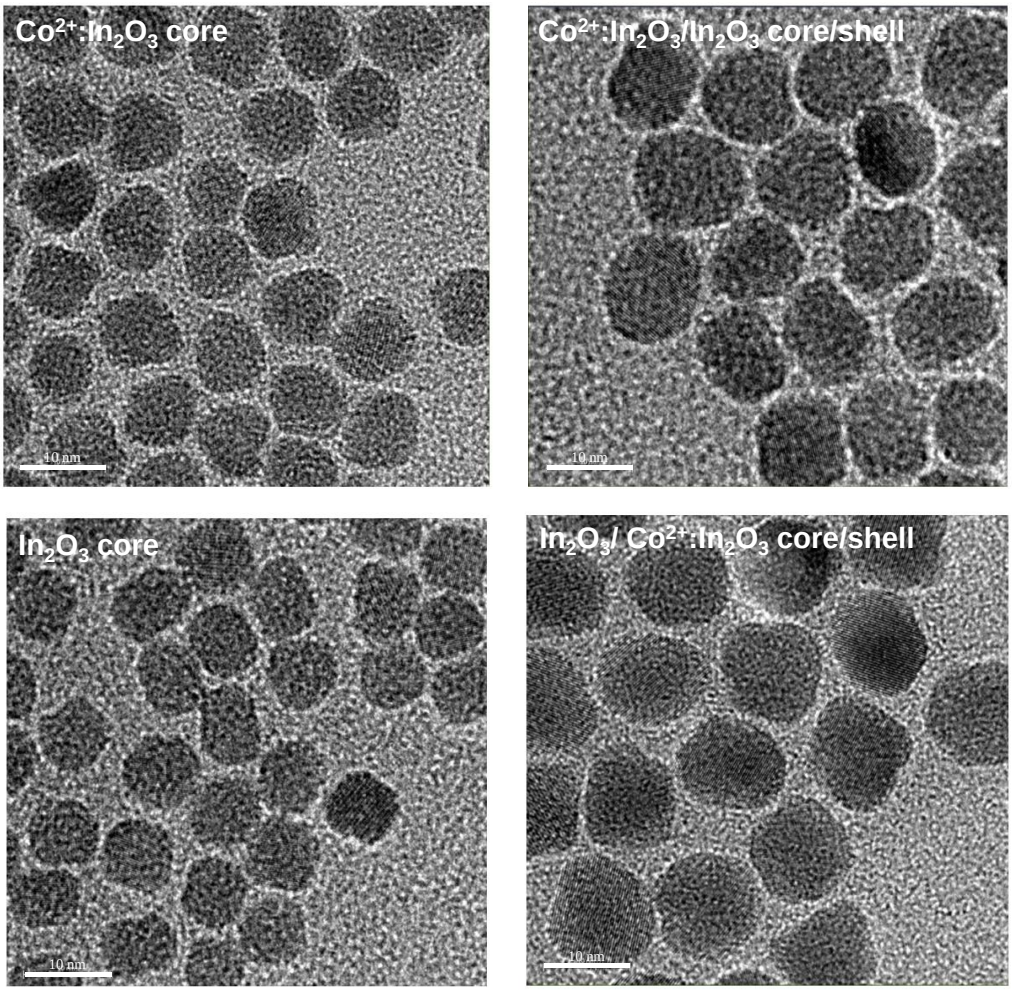

Figure 4.3 The HR-TEM images core-doped (top) and shell-doped (bottom) Co^{2+}:In_2O_3 NCs with both NC cores (left) and corresponding core/shell NC configurations (right) indicated in the figure. All scale bars are 10 nm.

Furthermore, the HR-TEM images in Figure 4.3 display the clear lattice fringes within individual NCs, indicating high crystallinity in both core and core/shell configurations. Based on the similarity in the lattice spacing measurements obtained from the HR-TEM images, it can be verified that both samples maintain the high-purity bcc-In_2O_3 structure.

4.2 Optical Properties of Core/Shell Co^{2+}:In_2O_3 NCs

The UV-Vis spectroscopy was utilized to explore the optical properties of core/shell

Co^{2+}:In_2O_3 NCs, focusing on understanding the effect of Co dopants and dopant locations in these NCs. The core-doped and shell-doped Co^{2+}:In_2O_3 NCs have similar doping concentrations but feature different locations for the Co dopants. According to the powder XRD patterns discussed before, both NC samples adopt the cubic phase In_2O_3 with no secondary phase formation. As described in the previous chapter, Co^{2+} ions, which have a smaller ionic radius (74.5 pm) [71] compared to In^{3+} ions (80 pm) [71] in an octahedral environment, are preferentially substituted for the *d* sites (highly distorted cation sites) in cubic bixbyite-type In_2O_3 structure. [55,58,61,70]

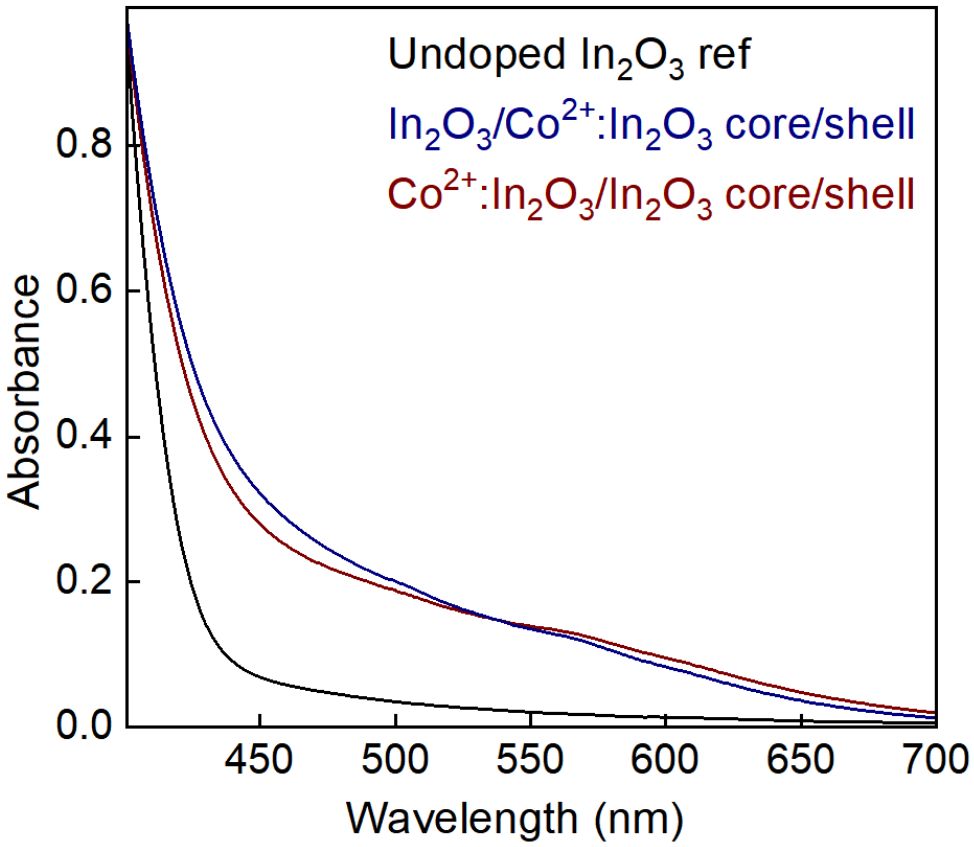

Figure 4.4 Normalized optical absorption spectrum of core-doped (brown trace) and shell-doped (blue trace) Co^{2+}:In_2O_3 NCs. The black trace indicates the spectrum of undoped In_2O_3 NCs prepared through one-pot synthesis method described in Experiment Section 2.2.1, for

comparison.

According to Figure 4.4, both core-doped and shell-doped samples display similar absorption band features with a series of weak transitions between 500 nm and 700 nm. These transitions are assigned to the spin-allowed ligand-field transitions of octahedral Co^{2+} ions similar to those observed in uniformly doped samples. However, due to the low concentrations of Co^{2+} dopants in these samples, only a shoulder peak feature can be clearly observed at around 560 nm, which can be assigned to the dominant transition, $^4T_1$ (F) → $^4T_1$ (P), which is indicative of the presence of Co within the Co^{2+}:In_2O_3 NC structure.[72,73] Moreover, when compared to uniformly-doped Co^{2+}:In_2O_3 sample with a similar overall doping concentration, the resemblance in spectra suggests no notable difference in optical properties, regardless of the dopant location in the In_2O_3 NCs.

4.3 Magneto-Optical Properties of Core/Shell Co^{2+}:In_2O_3 NCs

To explore the impact of cobalt dopant radial position on the magneto-optical properties and exchange interactions in the In_2O_3 NCs, MCD spectroscopy was employed. The study focused on comparing the MCD spectra of core-doped, shell-doped and uniformly-doped Co^{2+}:In_2O_3 NCs that have comparable concentrations of Co. Through this analysis, the effects of Co^{2+} dopant location and NC size on the excitonic Zeeman splitting of Co^{2+}:In_2O_3 NCs can be further investigated.

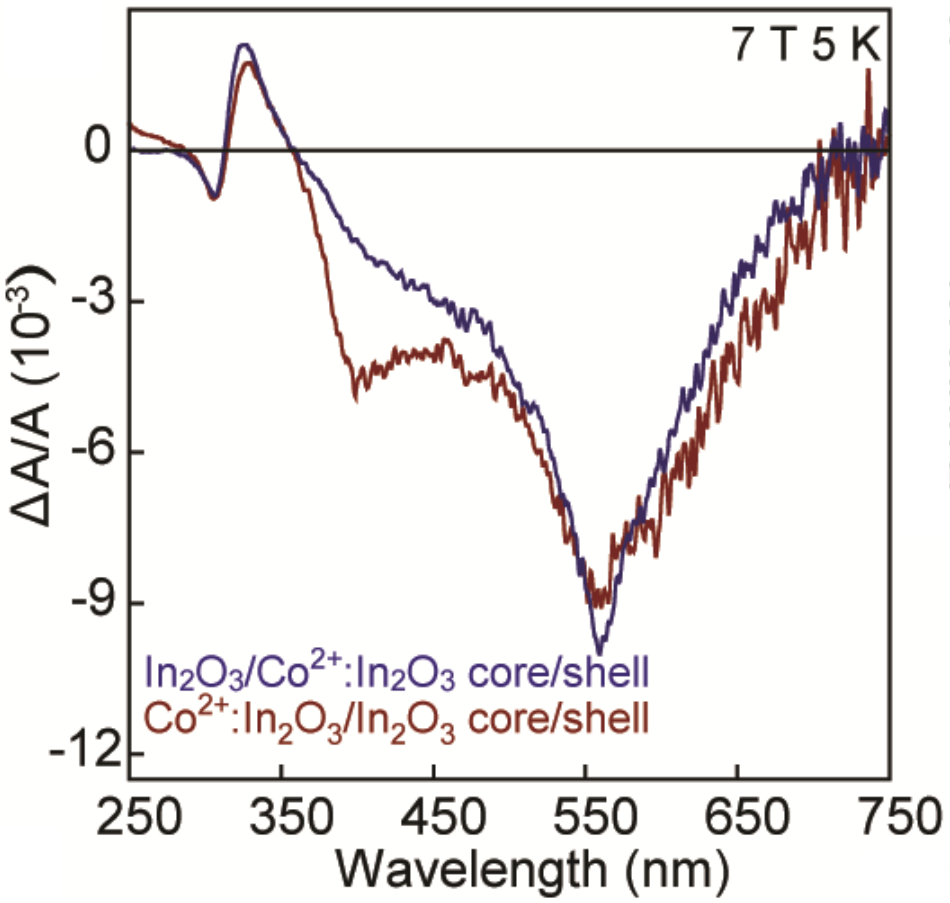

Figure 4.5 5 K-7 T full range normalized MCD spectra of $In_2O_3/Co^{2+}:In_2O_3$ (blue trace) and $Co^{2+}:In_2O_3/In_2O_3$ (brown trace) core/shell NCs. Both spectra were collected at 5 K under 7 T and converted to ΔA/A by dividing with corresponding absorbance in the same range.

Figure 4.5 shows the 5 K MCD spectra of core- and shell-doped $Co^{2+}:In_2O_3$ NCs collected under 7 T. The spectra are very similar in both Co^{2+} ligand-field and the band-gap range, indicating that dopants have similar speciation and similar effect on the excitonic splitting. In the Co^{2+} ligand field transition range, both samples exhibit similar MCD band features corresponding to the uniformly doped $Co^{2+}:In_2O_3$ NCs. It is noted that the transitions seen in the electronic absorption spectra are considerably more pronounced in 5 K-7 T MCD spectra. Similarly to the uniformly doped samples, the relatively sharp band at around 560 nm can be

assigned to the Co^{2+}-related $^4T_1$ (F) → $^4T_1$ (P) transition. This is accompanied by a series of less intense bands at shorter wavelengths, which probably originated from the spin-forbidden transitions to doublet states. [72,73] Besides, the trailing (red) edge between ca. 600 and 700 nm is consistent with the uniformly doped samples, which may be attributed to the $^4T_1$ → $^4A_2$ transition. However, due to the low Co^{2+} doping concentration, the specific features are not well defined. Additionally, the shell-doped sample also exhibits a shoulder band at ca. 390 nm with a relatively constant MCD intensity compared to the uniformly doped sample. As discussed in the previous chapter, this peak is hypothesized to be the charge transfer transition from the ligand O (2*p*) to Co^{2+} (3*d*) states.

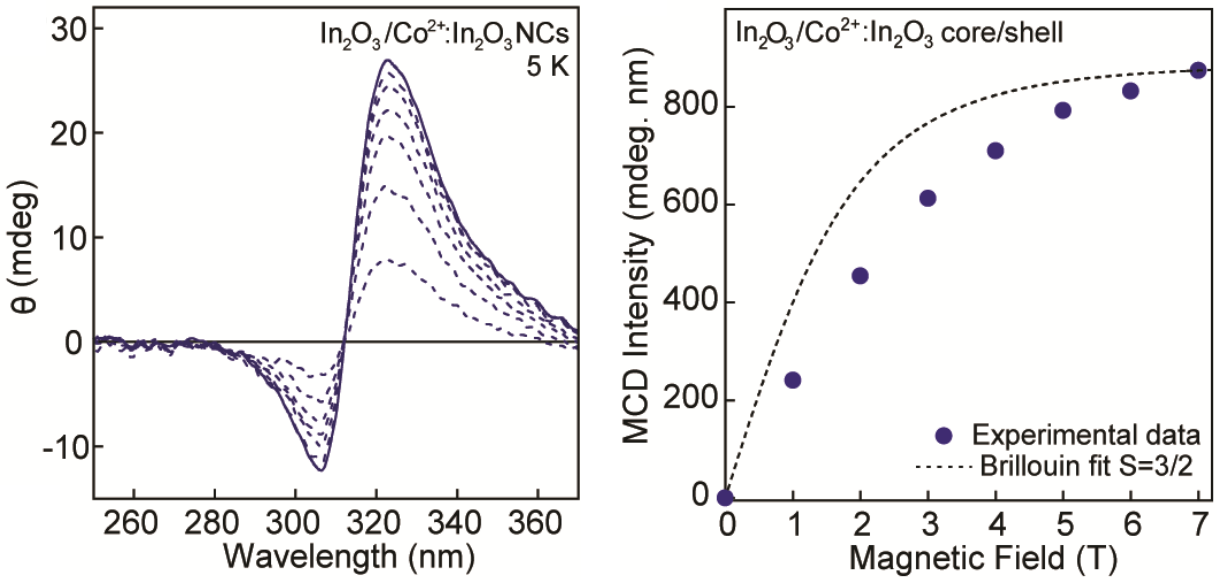

Figure 4.6 (Left) Variable-field (1-7 T) MCD spectra of $In_2O_3/Co^{2+}:In_2O_3$ core/shell NCs in the excitonic region. (Right) Variation of the integrated excitonic MCD intensity with magnetic field (blue spheres) and comparison with the Brillouin function for S = 3/2 and g = 2.002 (dashed black line).

Furthermore, field-dependent magneto-optical properties in the excitonic range were also

investigated (Figure 4.6 left). The variable-field MCD signal of the shell-doped Co^{2+}:In_2O_3 NCs exhibits a similar band shape to that of the uniformly-doped 1.97% Co^{2+}:In_2O_3 NCs. However, the excitonic MCD intensity clearly saturates at a lower rate with increasing magnetic field than expected for S = 3/2 (Figure 4.6 right), as observed for uniformly-doped NCs. Similarly, as shown in Figure 4.7, the core-doped Co^{2+}:In_2O_3 sample also displays a comparable band shape but a lower saturation rate with magnetic field compared to the uniformly doped NCs.

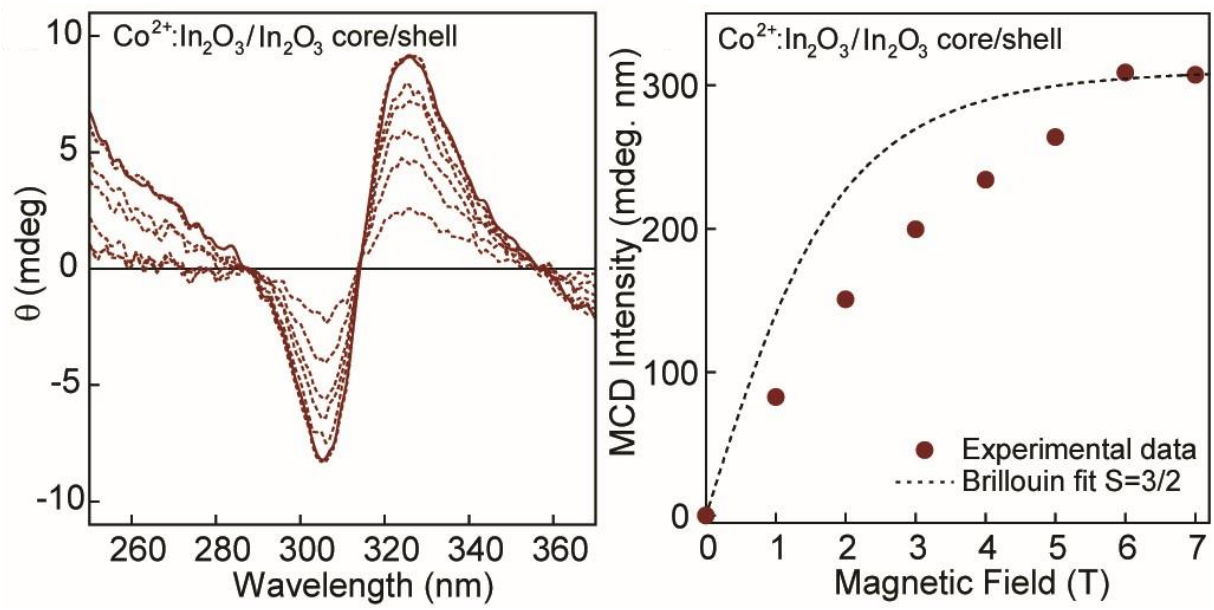

Figure 4.7 (Left) Variable-field (1-7 T) MCD spectra of Co^{2+}:In_2O_3/In_2O_3 core/shell NCs in the excitonic region. (Right) Variation of the integrated excitonic MCD intensity with magnetic field (blue spheres) and comparison with the Brillouin function for S = 3/2 and g = 2.002 (dashed black line).

These results suggest that there is an additional contribution to excitonic splitting in core/shell NCs arising from undoped region of the NCs, where the saturation follows S = 1/2 behavior (Figure 3.9). In In_2O_3/Co^{2+}:In_2O_3 NCs the native-defect-induced excitonic Zeeman splitting occurs mostly in the core, while the dopant-induced splitting occurs mostly in the shell

region. In Co^{2+}:In_2O_3/In_2O_3 NCs the splitting contributions are exactly the opposite. The MCD spectrum can therefore be represented as a superposition of the MCD spectra corresponding to the core and shell regions.

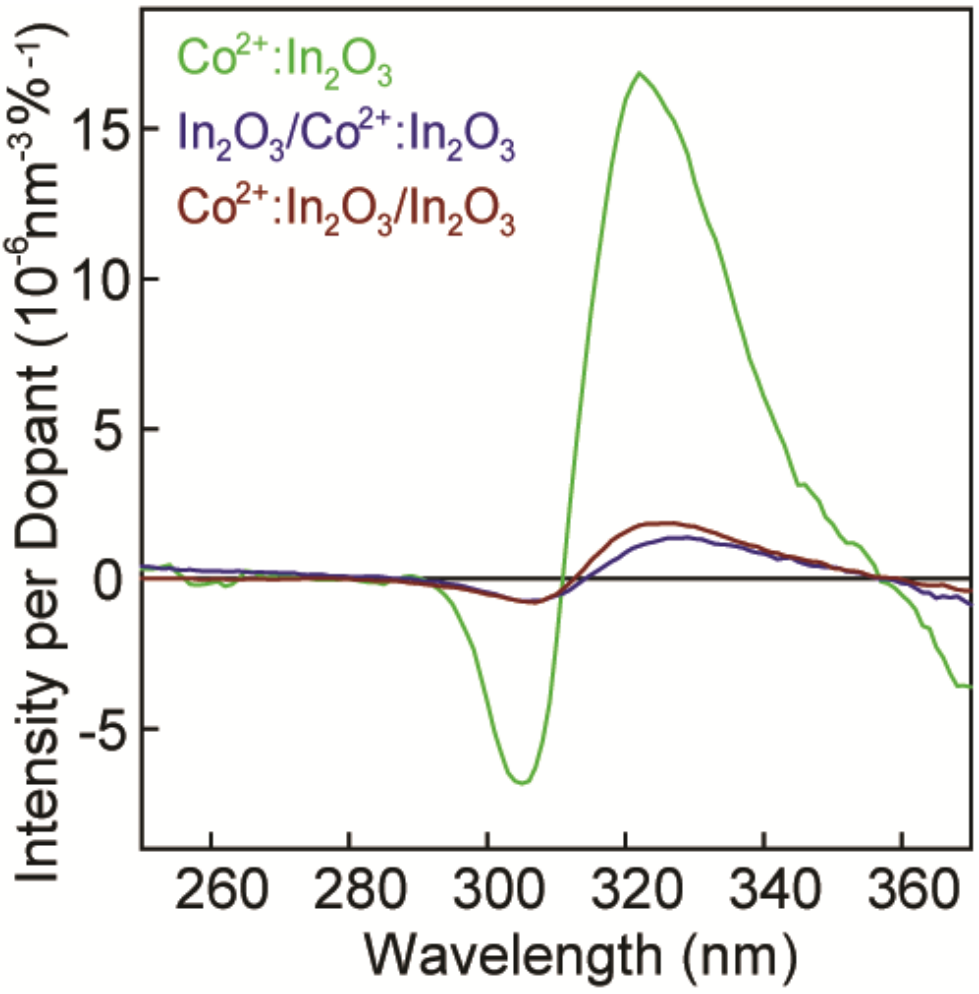

Figure 4.8 Comparison of the MCD spectra of Co^{2+}:In_2O_3 NCs normalized per volume and dopant for different radial placement of Co^{2+} ions, as indicated in the graph.

To quantitatively compare MCD spectra for different radial distributions of Co^{2+} dopants, it is necessary to normalize the $\Delta A/A$ to the volume of the NCs containing dopant ions. Furthermore, given the variation in the dopant concentration in the doped region of the NCs, the quantitative comparison must involve further normalization to the doping percentage.

Figure 4.8 compares the excitonic MCD intensities per dopant in the doped region for core/shell architectures and uniformly-doped NCs. There is only a small difference between the MCD signal intensities for core-doped and shell-doped NCs, indicating that the strength of exchange coupling between the exciton and Co^{2+} is not greatly affected by the radial position of the dopant for NCs having average sizes larger than ca. 10 nm.

However, the excitonic MCD intensity is nearly an order of magnitude larger for uniformly-doped NCs. The core/shell In_2O_3 NCs shown here are far from quantum confinement, which implies a weaker coupling regime relative to the analogous quantum dots.[81] Since the excitonic Bohr radius for In_2O_3 is much smaller than the size of the core/shell NCs, the excitonic wavefunction is also distributed more evenly throughout the NC, vanishing only at the very surface of the NCs. This leads to a significant overlap between the wavefunctions of the exciton and the Co^{2+} dopants even if the dopant centers are located in the shell region of the NCs. On the other hand, uniformly-doped NCs have an average radius of ca. 2.5 nm, which is comparable to the In_2O_3 Bohr radius.[84] The dopant-exciton coupling in this case is not only more sensitive to the dopant distribution, but also much stronger that in bulk, as it has been well-documented for Mn-doped II-VI NCs.[81,85] This leads to a larger dopant-induced excitonic Zeeman splitting in uniformly-doped NCs.

4.4 Conclusion

In this study, I explored the impact of Co^{2+} dopant placement and NC size on the magneto-optical properties of Co^{2+}:In_2O_3 NCs by comparing two distinct types of NCs to a uniformly-doped In_2O_3 sample at similar doping concentrations: one features a Co^{2+}-doped shell grown

on an undoped core, while the other has an undoped shell grown on a Co^{2+}-doped core. The results indicate that the strength of excitonic Zeeman splitting in large NCs (> ca. 10 nm) is minimally affected by dopant radial location due to the even spatial distribution of the excitonic wavefunction throughout the In_2O_3 NCs. However, in the case of small NCs comparable to the In_2O_3 Bohr radius, there is a notably strong dopant-exciton coupling, resulting in a drastic excitonic Zeeman splitting. Therefore, this research contributes to our understanding of how the dopant location and NC size influence the magneto-optical properties in Co^{2+}:In_2O_3 NCs, which will help with the development of In_2O_3-based DMSO materials and related potential spintronic applications.

Chapter 5

Conclusion and Future Work

5.1 Conclusion

The studies performed in this thesis focus on the manipulation of the exciton polarization in transition-metal-doped indium oxide NCs. Based on the studies mentioned above, I prepared the Co^{2+}:In_2O_3 NCs with varying Co concentrations by the one-pot colloidal synthesis method and characterized the crystal structure and elemental composition through XRD, TEM and ICP-OES measurements. The magneto-optical behavior of Co^{2+}:In_2O_3 NC samples were investigated by MCD spectroscopy. Comparison of the MCD spectra of different samples suggests that there is a competition between excitonic splitting induced by intrinsic defects, such as singly charged oxygen vacancies, and extrinsic Co^{2+} substitutional doping of In_2O_3 NC lattice. Co^{2+} dopants undergo spin exchange interactions with the host-lattice charge carriers that are of similar strength as the spin-exchange interactions involving intrinsic defects. The two types of exchange interactions are found to be comparable in magnitude but result in the opposite splitting pattern of the band states. The band splitting in undoped and lightly-doped NCs is, therefore, dominated by exchange interactions involving singly-charged oxygen vacancies in the presence of an applied magnetic field. With increasing Co doping level, the dopant-induced exchange interactions take over as the dominant mechanism governing the anomalous Zeeman splitting of the NC band states. This competition between the two contributions leads to an anomalous behavior, including the cancelation of the MCD signal for Co^{2+} doping concentration of ca. 0.5 % (~12 dopants per 5 nm diameter NC). Furthermore,

evidence also suggests that the magnitude and the underlying mechanism of the excitonic Zeeman splitting are not drastically impacted by the radial location of the dopants in large NCs (> ca. 10 nm), which is rationalized in terms of relatively even spatial distribution of the excitonic wavefunction throughout the NC in the absence of quantum confinement in In_2O_3 NCs. Importantly, the overall coupling between exciton and dopants, and therefore, the magnitude of the excitonic Zeeman splitting per dopant ion, is significantly stronger in uniformly-doped than in core- or shell-doped NCs, owing to a spatial confinement of the excitonic wavefunction. The results of this work provide a new understanding of the properties of DMSO NCs, and the challenges associated with predicting and consistently reproducing their behavior. Consideration of the contributions to excitonic Zeeman splitting identified in this work allow for a design of DMSO NCs with improved characteristics for spintronics and quantum information technologies.

5.2 Future Work

To verify that the generality of the obtained results, which is the competition between the Zeeman effect involving intrinsic defects and magnetic dopants on the exciton polarization in In_2O_3 DMSO NCs, further research was conducted on NCs doped with different transition metals. Thus, I prepared another set of Ni^{2+}-doped In_2O_3 (Ni^{2+}:In_2O_3) NCs using the same synthesis method with $Ni(acac)_2$ as the Ni^{2+} precursor. This approach aims to explore whether the magneto-optical behavior and exciton polarization seen in Co^{2+}:In_2O_3 NCs are also present in In_2O_3 NCs doped with Ni, therefore extending the understanding of these phenomena to a broader range of transition metal-doped In_2O_3 materials.

In this new set of experiments, I conducted a preliminary characterization of Ni^{2+}:In_2O_3 NC samples with XRD and ICP-OES measurements. The XRD patterns, as shown in Figure 5.1, indicate that all Ni-doped samples consist of high-purity cubic-phase In_2O_3 NCs, without any detectable side products. Notably, an increased broadening of the characteristic peaks with higher Ni doping concentrations suggests a decrease in average NC sizes, associated with the incorporation of more Ni^{2+} ions into the In_2O_3 lattice. This observation is consistent with the trend seen in Co-doped samples, where smaller dopant ions are substituted into the In^{3+} cation sites.

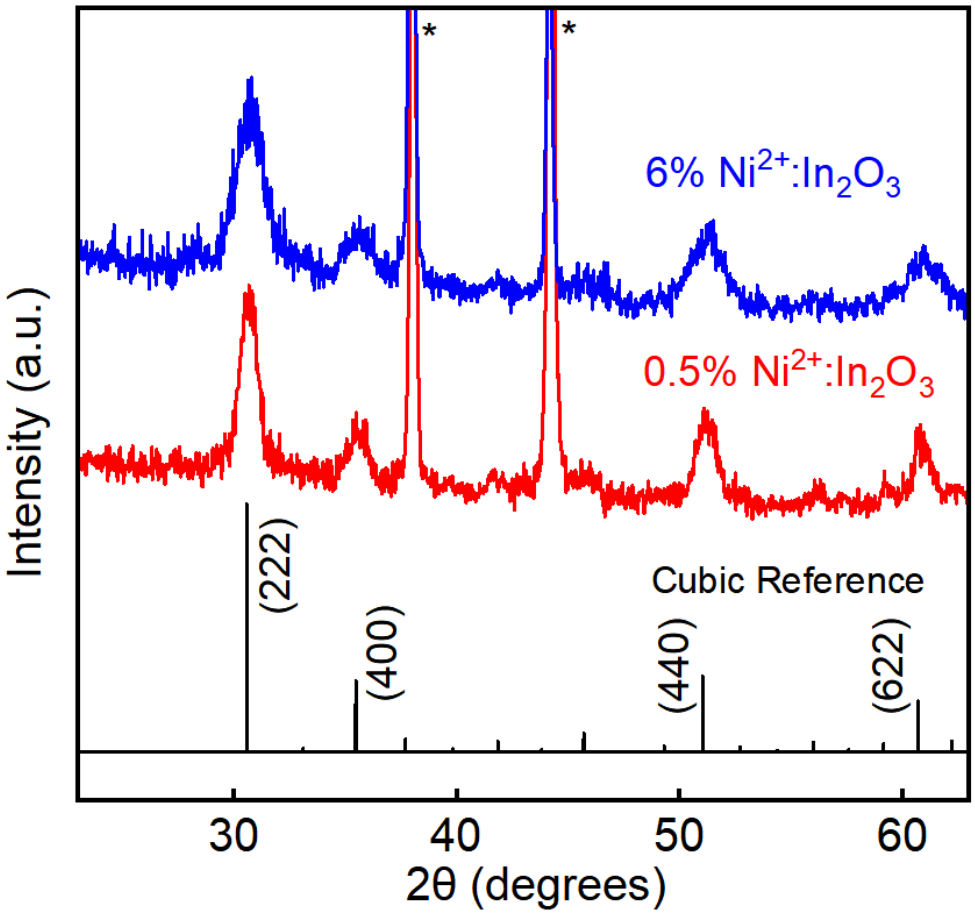

Figure 5.1 Powder XRD patterns of Ni^{2+}:In_2O_3 NCs with the doping concentration indicated in the graph. Sharp peaks marked with * represent the Al substrate. The black pattern is the

reference XRD pattern of cubic bixbyite In_2O_3 (JCPDS No.88-2160).

Furthermore, ICP-OES analysis reveals that the actual concentration of Ni in the doped samples closely matches the precursor ratio, confirming successful incorporation of Ni^{2+} ions into the In_2O_3 NCs.

Based on the preliminary structural characterization of the Ni^{2+}:In_2O_3 NCs, these new samples have demonstrated a promising extension to the research presented in this thesis. Consequently, further analysis of the optical and magneto-optical properties of Ni^{2+}:In_2O_3 NCs becomes increasingly intriguing. The next part of research is crucial to ascertain whether the mechanisms obtained from the Co^{2+}:In_2O_3 NCs are universally applicable, thereby enriching our understanding of DMSOs. This research will not only validate existing theories but also potentially reveal new insights into the behavior of DMSOs under various doping conditions. The outcomes of these studies are expected to lay a foundational groundwork for future applications and innovations in the field, potentially leading to breakthroughs in areas like spintronics and quantum computing where DMSOs could play a pivotal role.

Reference

1. Salonitis, K.; Pandremenos, J.; Paralikas, J.; Chryssolouris, G. (2010). Multifunctional Materials: Engineering Applications and Processing Challenges. *The International Journal of Advanced Manufacturing Technology*, **49**, 803-826.

2. Awschalom, D. D.; Flatté, M. E. (2007). Challenges for Semiconductor Spintronics. *Nature Physics*, **3**(3), 153-159.

3. Žutić, I.; Fabian, J.; Sarma, S. D. (2004). Spintronics: Fundamentals and Applications. *Reviews of Modern Physics*, **76**(2), 323.

4. Ando, K. (2006). Seeking Room-Temperature Ferromagnetic Semiconductors. *Science*, **312**(5782), 1883-1885.

5. Wolf, S. A.; Awschalom, D. D.; Buhrman, R. A.; Daughton, J. M.; von Molnár, V. S.; Roukes, M. L.; et al. (2001). Spintronics: a Spin-Based Electronics Vision for the Future. *Science*, **294**(5546), 1488-1495.

6. Baibich, M. N.; Broto, J. M.; Fert, A.; Van Dau, F. N.; Petroff, F.; Etienne, P.; et al. (1988). Giant Magnetoresistance of (001)Fe/(001)Cr Magnetic Superlattices. *Physical Review Letters*, **61**(21), 2472.

7. Binasch, G.; Grünberg, P.; Saurenbach, F.; Zinn, W. (1989). Enhanced Magnetoresistance in Layered Magnetic Structures with Antiferromagnetic Interlayer Exchange. *Physical Review B*, **39**(7), 4828.

8. Berger, L. I. (2020). *Semiconductor Materials.* CRC press.

9. Gaj, J. A. (1999). Semimagnetic Semiconductors. *Acta Physica Polonica A*, **96**(5), 651-664.

10. Ohno, H. (1998). Making Nonmagnetic Semiconductors Ferromagnetic. *Science*, **281**(5379), 951-956.

11. Furdyna, J. K. (1988). Diluted Magnetic Semiconductors. *Journal of Applied Physics*, **64**(4), R29-R64.

12. Jungwirth, T.; Wang, K. Y.; Mašek, J.; Edmonds, K. W.; König, J.; Sinova, J.; et al. (2005). Prospects for High Temperature Ferromagnetism in (Ga, Mn) As semiconductors. *Physical Review B*, **72**(16), 165204.

13. Dobrowolska, M.; Tivakornsasithorn, K.; Liu, X.; Furdyna, J. K.; Berciu, M.; Yu, K. M.; et al. (2012). Controlling the Curie Temperature in (Ga,Mn)As through Location of the Fermi Level within the Impurity Band. *Nature Materials*, **11**(5), 444-449.

14. Sonoda, S.; Shimizu, S.; Sasaki, T.; Yamamoto, Y.; Hori, H. (2002). Molecular Beam Epitaxy of Wurtzite (Ga,Mn)N Films on Sapphire (0001) Showing the Ferromagnetic Behaviour at Room Temperature. *Journal of Crystal Growth*, **237**, 1358-1362.

15. Novák, V.; Olejník, K.; Wunderlich, J.; Cukr, M.; Výborný, K.; Rushforth, A. W.; et al. (2008). Curie Point Singularity in the Temperature Derivative of Resistivity in (Ga,Mn)As. *Physical Review Letters*, **101**(7), 077201.

16. Hegde, M.; Farvid, S. S.; Hosein, I. D.; Radovanovic, P. V. (2011). Tuning Manganese Dopant Spin Interactions in Single GaN Nanowires at Room Temperature. *ACS Nano*, **5**(8), 6365-6373.

17. Coey, J. M. D.; Venkatesan, M.; Fitzgerald, C. B. (2005). Donor Impurity Band Exchange in Dilute Ferromagnetic Oxides. *Nature Materials*, **4**(2), 173-179.

18. Calderon, M. J.; Sarma, S. D. (2007). Theory of Carrier Mediated Ferromagnetism in Dilute Magnetic Oxides. *Annals of Physics*, **322**(11), 2618-2634.

19. Wang, Z.; Dong, X.; Chen, Z.; Xiong, H.; Gao, J.; Du, J.; et al. (2021). Dependence of the Ferromagnetism on Vacancy Defect in Annealed In_2O_3 Nanocrystals: A Positron Annihilation Study. *Physica Status Solidi (a)*, **218**(6), 2000631.

20. Matsumoto, Y.; Murakami, M.; Shono, T.; Hasegawa, T.; Fukumura, T.; Kawasaki, M.; et al. (2001). Room-Temperature Ferromagnetism in Transparent Transition Metal-Doped Titanium Dioxide. *Science*, **291**(5505), 854-856.

21. Coey, J. M. D.; Sanvito, O. S. (2004). Magnetic Semiconductors and Half-Metals. *Journal of Physics D: Applied Physics*, **37**(7), 988.

22. Ginley, D. S.; Bright, C. (2000). Transparent Conducting Oxides. *MRS Bulletin*, **25**(8), 15-18.

23. Prellier, W.; Fouchet, A.; Mercey, B. (2003). Oxide-Diluted Magnetic Semiconductors: a Review of the Experimental Status. *Journal of Physics: Condensed Matter*, **15**(37), R1583.

24. Zhang, C.; Yin, P.; Lu, W.; Galievsky, V.; Radovanovic, P. V. (2021). On the Origin of d^0 Magnetism in Transparent Metal Oxide Nanocrystals. *The Journal of Physical Chemistry C*, **125**(50), 27714-27722.

25. Dave, N.; Pautler, B. G.; Farvid, S. S.; Radovanovic, P. V. (2010). Synthesis and Surface Control of Colloidal Cr^{3+}-doped SnO_2 Transparent Magnetic Semiconductor Nanocrystals. *Nanotechnology*, **21**(13), 134023.

26. Fukumura, T.; Kawasaki, M. (2013). Magnetic Oxide Semiconductors: On the High-Temperature Ferromagnetism in TiO_2- and ZnO-Based Compounds. *Functional Metal Oxides: New Science and Novel Applications*, 89-131.

27. Sato, K.; Katayama-Yoshida, H. (2001). Ferromagnetism in a Transition Metal Atom Doped ZnO. *Physica E: Low-dimensional Systems and Nanostructures*, **10**(1-3), 251-255.

28. Hakimi, A. M. H. R.; Blamire, M. G.; Heald, S. M.; Alshammari, M. S.; Alqahtani, M. S.; Score, D. S.; et al. (2011). Donor-Band Ferromagnetism in Cobalt-Doped Indium Oxide. *Physical Review B*, **84**(8), 085201.

29. Farvid, S. S.; Hegde, M.; Radovanovic, P. V. (2013). Influence of the Host Lattice Electronic Structure on Dilute Magnetic Interactions in Polymorphic Cr(III)-Doped In_2O_3 Nanocrystals. *Chemistry of Materials*, **25**(2), 233-244.

30. Farvid, S. S.; Ju, L.; Worden, M.; Radovanovic, P. V. (2008). Colloidal Chromium-Doped In_2O_3 Nanocrystals as Building Blocks for High-Tc Ferromagnetic Transparent Conducting Oxide Structures. *The Journal of Physical Chemistry C*, **112**(46), 17755-17759.

31. Jaffe, J. E.; Droubay, T. C.; Chambers, S. A. (2005). Oxygen Vacancies and Ferromagnetism in $Co_xTi_{1-x}O_{2-x-y}$. *Journal of Applied Physics*, **97**(7).

32. Shinde, S. R.; Ogale, S. B.; Sarma, S. D.; Simpson, J. R.; Drew, H. D.; Lofland, S. E.; et al. (2003). Ferromagnetism in Laser Deposited Anatase $Ti_{1-x}Co_xO_{2-\delta}$ Films. *Physical Review B*, **67**(11), 115211.

33. Stoneham, M. (2010). The Strange Magnetism of Oxides and Carbons. *Journal of Physics: Condensed Matter*, **22**(7), 074211.

34. Ghosh, S.; Khan, G. G.; Das, B.; Mandal, K. (2011). Vacancy-Induced Intrinsic d^0 Ferromagnetism and Photoluminescence in Potassium Doped ZnO Nanowires. *Journal of Applied Physics*, **109**(12).

35. Venkatesan, M.; Fitzgerald, C. B.; Coey, A. J. (2004). Unexpected Magnetism in a Dielectric Oxide. *Nature*, **430**(7000), 630-630.

36. Ackland, K.; Coey, J. M. D. (2018). Room Temperature Magnetism in CeO_2—A Review. *Physics Reports*, **746**, 1-39.

37. Khan, G. G.; Ghosh, S.; Sarkar, A.; Mandal, G.; Mukherjee, G. D.; Manju, U.; et al. (2015). Defect Engineered d^0 Ferromagnetism in Tin-Doped Indium Oxide Nanostructures and Nanocrystalline Thin-Films. *Journal of Applied Physics*, **118**(7).

38. Xiao, Z. R.; Fan, X. F.; Guan, L. X.; Huan, C. H. A.; Kuo, J. L.; Wang, L. (2009). First-Principles Study of the Magnetization of Oxygen-Depleted In_2O_3 (001) Surfaces. *Journal of Physics: Condensed Matter*, **21**(27), 272202.

39. Singh, S. B.; Wang, Y. F.; Shao, Y. C.; Lai, H. Y.; Hsieh, S. H.; Limaye, M. V.; et al. (2014). Observation of the Origin of d^0 Magnetism in ZnO Nanostructures Using X-Ray-Based Microscopic and Spectroscopic Techniques. *Nanoscale*, **6**(15), 9166-9176.

40. Liu, W.; Li, W.; Hu, Z.; Tang, Z.; Tang, X. (2011). Effect of Oxygen Defects on Ferromagnetic of Undoped ZnO. *Journal of Applied Physics*, **110**(1).

41. Santara, B.; Giri, P. K.; Imakita, K.; Fujii, M. (2013). Evidence of Oxygen Vacancy Induced Room Temperature Ferromagnetism in Solvothermally Synthesized Undoped TiO_2 Nanoribbons. *Nanoscale*, **5**(12), 5476-5488.

42. Coey, J. M. D. (2006). Dilute Magnetic Oxides. *Current Opinion in Solid State and Materials Science*, **10**(2), 83-92.

43. Spaldin, N. A. (2010). *Magnetic Materials: Fundamentals and Applications.* Cambridge University Press.

44. Coey, J. M. D.; Wongsaprom, K.; Alaria, J.; Venkatesan, M. (2008). Charge-Transfer Ferromagnetism in Oxide Nanoparticles. *Journal of Physics D: Applied Physics*, **41**(13), 134012.

45. Priour Jr, D. J.; Sarma, S. D. (2006). Phase Diagram of the Disordered RKKY Model in Dilute Magnetic Semiconductors. *Physical Review Letters*, **97**(12), 127201.

46. Coey, J. M. D.; Douvalis, A. P.; Fitzgerald, C. B.; Venkatesan, M. (2004). Ferromagnetism in Fe-doped SnO_2 Thin Films. *Applied Physics Letters*, **84**(8), 1332-1334.

47. Farvid, S. S.; Dave, N.; Radovanovic, P. V. (2010). Phase-Controlled Synthesis of Colloidal In_2O_3 Nanocrystals via Size-Structure Correlation. *Chemistry of Materials*, **22**(1), 9-11.

48. Farvid, S. S.; Radovanovic, P. V. (2012). Phase Transformation of Colloidal In_2O_3 Nanocrystals Driven by the Interface Nucleation Mechanism: a Kinetic Study. *Journal of the American Chemical Society*, **134**(16), 7015-7024.

49. Hutfluss, L. N.; Radovanovic, P. V. (2015). Controlling the Mechanism of Phase Transformation of Colloidal In_2O_3 Nanocrystals. *Journal of the American Chemical Society*, **137**(3), 1101-1108.

50. Tandon, B.; Shanker, G. S.; Nag, A. (2014). Multifunctional Sn- and Fe-Codoped In_2O_3 Colloidal Nanocrystals: Plasmonics and Magnetism. *The journal of physical chemistry letters*, **5**(13), 2306-2311.

51. Tandon, B.; Yadav, A.; Nag, A. (2016). Delocalized Electrons Mediated Magnetic Coupling in Mn–Sn Codoped In_2O_3 Nanocrystals: Plasmonics Shows the Way. *Chemistry of Materials*, **28**(11), 3620-3624.

52. Mason, T. O.; Gonzalez, G. B.; Hwang, J. H.; Kammler, D. R. (2003). Point Defects and Related Properties of Highly Co-Doped Bixbyite In_2O_3. *Physical Chemistry Chemical Physics*, **5**(11), 2183-2189.

53. Babu, S. H.; Kaleemulla, S.; Rao, N. M.; Krishnamoorthi, C. (2016). Indium Oxide: A Transparent, Conducting Ferromagnetic Semiconductor for Spintronic Applications. *Journal of Magnetism and Magnetic Materials*, **416**, 66-74.

54. González, G. B. (2012). Investigating the Defect Structures in Transparent Conducting Oxides Using X-ray and Neutron Scattering Techniques. *Materials*, **5**(5), 818-850.

55. Stanek, C. R.; McClellan, K. J.; Uberuaga, B. P.; Sickafus, K. E.; Levy, M. R.; Grimes, R. W. (2007). Determining the Site Preference of Trivalent Dopants in Bixbyite Sesquioxides by Atomic-Scale Simulations. *Physical Review B*, **75**(13), 134101.

56. Mason, W. R. (2007). *Magnetic Circular Dichroism Spectroscopy.* John Wiley & Sons.

57. Piepho, S. B.; Schatz, P. N. (1983). Group Theory in Spectroscopy: with Applications to Magnetic Circular Dichroism. *Wiley-Interscience Monographs in Chemical Physics*.

58. Farvid, S. S.; Sabergharesou, T.; Hutfluss, L. N.; Hegde, M.; Prouzet, E.; Radovanovic, P. V. (2014). Evidence of Charge-Transfer Ferromagnetism in Transparent Diluted Magnetic Oxide Nanocrystals: Switching the Mechanism of Magnetic Interactions. *Journal of the American Chemical Society*, **136**(21), 7669-7679.

59. Zorn, S. (2023). *Investigation of the Electronic Structure and Magnetic Properties of* CeO_{2-X} (Master's thesis, University of Waterloo).

60. Tandon, B.; Yadav, A.; Khurana, D.; Reddy, P.; Santra, P. K.; Nag, A. (2017). Size-Induced Enhancement of Carrier Density, LSPR Quality Factor, and Carrier Mobility in Cr–Sn doped In_2O_3 Nanocrystals. *Chemistry of Materials*, **29**(21), 9360-9368.

61. Jansons, A. W.; Koskela, K. M.; Crockett, B. M.; Hutchison, J. E. (2017). Transition Metal-Doped Metal Oxide Nanocrystals: Efficient Substitutional Doping through a Continuous Growth Process. *Chemistry of Materials*, **29**(19), 8167-8176.

62. Yin, P.; Tan, Y.; Fang, H.; Hegde, M.; Radovanovic, P. V. (2018). Plasmon-Induced Carrier Polarization in Semiconductor Nanocrystals. *Nature Nanotechnology*, **13**(6), 463-467.

63. Murali, A.; Barve, A.; Leppert, V. J.; Risbud, S. H.; Kennedy, I. M.; Lee, H. W. (2001).

Synthesis and Characterization of Indium Oxide Nanoparticles. *Nano Letters*, **1**(6), 287-289.

64. Barrows, C. J.; Vlaskin, V. A.; Gamelin, D. R. (2015). Absorption and Magnetic Circular Dichroism Analyses of Giant Zeeman Splittings in Diffusion-Doped Colloidal $Cd_{1-x}Mn_xSe$ Quantum Dots. *The Journal of Physical Chemistry Letters*, **6**(15), 3076-3081.

65. Archer, P. I.; Santangelo, S. A.; Gamelin, D. R. (2007). Inorganic Cluster Syntheses of TM^{2+}-doped Quantum Dots (CdSe, CdS, CdSe/CdS): Physical Property Dependence on Dopant Locale. J*ournal of the American Chemical Society*, **129**(31), 9808-9818.

66. Schwartz, D. A.; Norberg, N. S.; Nguyen, Q. P.; Parker, J. M.; Gamelin, D. R. (2003). Magnetic Quantum Dots: Synthesis, Spectroscopy, and Magnetism of Co^{2+}- and Ni^{2+}-Doped ZnO Nanocrystals. *Journal of the American Chemical Society*, **125**(43), 13205-13218.

67. Yang, Y.; Jin, Y.; He, H.; Wang, Q.; Tu, Y.; Lu, H.; et al. (2010). Dopant-Induced Shape Evolution of Colloidal Nanocrystals: the Case of Zinc Oxide. *Journal of the American Chemical Society*, **132**(38), 13381-13394.

68. Guria, A. K.; Pradhan, N. (2016). Doped or not Doped: Ionic Impurities for Influencing the Phase and Growth of Semiconductor Nanocrystals. *Chemistry of Materials*, **28**(15), 5224-5237.

69. Fang, H.; Hegde, M.; Yin, P.; Radovanovic, P. V. (2017). Tuning Plasmon Resonance of In_2O_3 Nanocrystals throughout the Mid-Infrared Region by Competition between Electron Activation and Trapping. *Chemistry of Materials*, **29**(11), 4970-4979.

70. Raebiger, H.; Lany, S.; Zunger, A. (2009). Electronic Structure, Donor and Acceptor Transitions, and Magnetism of 3*d* Impurities in In_2O_3 and ZnO. *Physical Review B*, **79**(16), 165202.

71. Shannon, R. T.; Prewitt, C. T. (1969). Effective Ionic Radii in Oxides and Fluorides.

Acta Crystallographica Section B: Structural Crystallography and Crystal Chemistry, **25**(5), 925-946.

72. Gailey, K. D.; Palmer, R. A. (1972). Natural Circular Dichroism of $[Co(H_2O)_6]^{2+}$ and $[Cu(H_2O)_6]^{2+}$ in a Chiral Lattice. *Chemical Physics Letters*, **13**(2), 176-180.

73. Lever, A. P. (1984). Inorganic Electronic Spectroscopy. *Studies in Physical and Theoretical Chemistry*, **33**.

74. Garnet, N. S.; Ghodsi, V.; Hutfluss, L. N.; Yin, P.; Hegde, M.; Radovanovic, P. V. (2017). Probing the Role of Dopant Oxidation State in the Magnetism of Diluted Magnetic Oxides Using Fe-Doped In_2O_3 and SnO_2 Nanocrystals. *The Journal of Physical Chemistry C*, **121**(3), 1918-1927.

75. Tandon, B.; Radovanovic, P. V. (2023). Size Control of the Mechanism of Exciton Polarization in Metal Oxide Nanocrystals through Fermi Level Pinning. *ACS Nano*, **17**(14), 14069-14078.

76. Yin, P.; Hegde, M.; Tan, Y.; Chen, S.; Garnet, N.; Radovanovic, P. V. (2018). Controlling the Mechanism of Excitonic Splitting in In_2O_3 Nanocrystals by Carrier Delocalization. *ACS Nano*, **12**(11), 11211-11218.

77. Walsh, A.; Sokol, A. A.; Catlow, C. R. A. (2011). Free Energy of Defect Formation: Thermodynamics of Anion Frenkel Pairs in Indium Oxide. *Physical Review B*, **83**(22), 224105.

78. Radovanovic, P. V. (2013). Defect-Induced Optical and Magnetic Properties of Colloidal Transparent Conducting Oxide Nanocrystals. *Functional Metal Oxides: New Science and Novel Applications*, 163-194.

79. Clabau, F.; Rocquefelte, X.; Le Mercier, T.; Deniard, P.; Jobic, S.; Whangbo, M. H. (2006). Formulation of Phosphorescence Mechanisms in Inorganic Solids Based on a New

Model of Defect Conglomeration. *Chemistry of Materials*, **18**(14), 3212-3220.

80. Wang, T.; Layek, A.; Hosein, I. D.; Chirmanov, V.; Radovanovic, P. V. (2014). Correlation Between Native Defects and Dopants in Colloidal Lanthanide-Doped Ga_2O_3 Nanocrystals: a Path to Enhance Functionality and Control Optical Properties. *Journal of Materials Chemistry C*, **2**(17), 3212-3222.

81. Barrows, C. J.; Fainblat, R.; Gamelin, D. R. (2017). Excitonic Zeeman Splittings in Colloidal CdSe Quantum Dots Doped with Single Magnetic Impurities. *Journal of Materials Chemistry C*, **5**(21), 5232-5238.

82. Gibbs, S. L.; Dean, C.; Saad, J.; Tandon, B.; Staller, C. M.; Agrawal, A.; et al. (2020). Dual-Mode Infrared Absorption by Segregating Dopants within Plasmonic Semiconductor Nanocrystals. *Nano Letters*, **20**(10), 7498-7505.

83. Crockett, B. M.; Jansons, A. W.; Koskela, K. M.; Johnson, D. W.; Hutchison, J. E. (2017). Radial Dopant Placement for Tuning Plasmonic Properties in Metal Oxide Nanocrystals. *ACS Nano*, **11**(8), 7719-7728.

84. Guha, P.; Kar, S.; Chaudhuri, S. (2004). Direct Synthesis of Single Crystalline In_2O_3 Nanopyramids and Nanocolumns and Their Photoluminescence Properties. *Applied Physics Letters*, **85**(17), 3851-3853.

85. Bhattacharjee, A. K.; Pérez-Conde, J. (2003). Optical Properties of Paramagnetic Ion-Doped Semiconductor Nanocrystals. *Physical Review B*, **68**(4), 045303.